Received: 20 December 2017 | Revised: 23 May 2018 | Accepted: 5 June 2018
DOI: 10.1002/eqe.3072

RESEARCH ARTICLE

WILEY

Seismic performance evaluation of single damped-outrigger system incorporating buckling-restrained braces

Pao-Chun Lin | Toru Takeuchi | Ryota Matsui

Department of Architecture and Building Engineering, Tokyo Institute of Technology, Tokyo, Japan

Correspondence
Toru Takeuchi, Department of Architecture and Building Engineering, Tokyo Institute of Technology, Tokyo, Japan.
Email: takeuchi.t.ab@m.titech.ac.jp

Summary

The outrigger system is an effective means of controlling the seismic response of core-tube type tall buildings by mobilizing the axial stiffness of the perimeter columns. This study investigates the damped-outrigger, incorporating the buckling-restrained brace (BRB) as energy dissipation device (BRB-outrigger system). The building's seismic responses are expected to be effectively reduced because of the high BRB elastic stiffness during minor earthquakes and through the stable energy dissipation mechanism of the BRB during large earthquakes. The seismic behavior of the BRB-outrigger system was investigated by performing a spectral analysis considering the equivalent damping to incorporate the effects of BRB inelastic deformation. Nonlinear response history analyses were performed to verify the spectral analysis results. The analytical models with building heights of 64, 128, and 256 m were utilized to investigate the optimal outrigger elevation and the relationships between the outrigger truss flexural stiffness, BRB axial stiffness, and perimeter column axial stiffness to achieve the minimum roof drift and acceleration responses. The method of determining the BRB yield deformation and its effect on overall seismic performance were also investigated. The study concludes with a design recommendation for the single BRB-outrigger system.

KEYWORDS
buckling-restrained brace, optimal design, outrigger, parametric analysis, spectral analysis

1 | INTRODUCTION

The outrigger system has been widely adopted in tall core-tube type buildings around the world.[1,2] The traditional outrigger mitigates building seismic responses by increasing the system stiffness. However, the increased stiffness may also amplify the acceleration response. Figure 1A and B shows a typical building elevation with a single outrigger, and the floor framing plan on the outrigger floor. The core structure provides most of the lateral force resistance capacity, and the perimeter columns are responsible for supporting the gravity loads. When the building deforms horizontally (Figure 1C), the core structure's flexural deformation triggers the relatively stiff outrigger truss to rotate. The outrigger truss then triggers additional extension or compression on the perimeter columns below the outrigger. By mobilizing the axial stiffness of the perimeter columns, the flexural demand on the core structure can be reduced. However, the elastic design concept of outrigger may result in large force demands on the outrigger members, increasing both complexity and costs in engineering practices.[3]

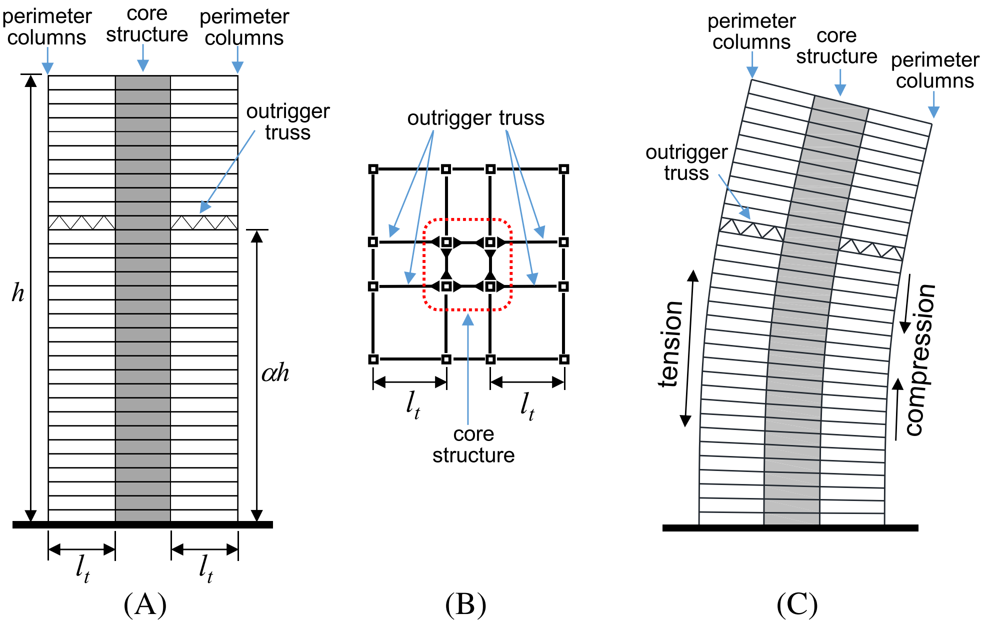

FIGURE 1 A, Elevation, B, floor framing plan on outrigger floor, and C, outrigger truss mobilizing perimeter column axial stiffness [Colour figure can be viewed at wileyonlinelibrary.com]

The concept of a damped-outrigger has been proposed[4-7] to increase the damping, instead of increasing the stiffness, by inserting energy dissipation devices at the outrigger truss ends. The dampers dissipate energy through the relative movements between outrigger truss ends and the perimeter columns. The optimal damped-outrigger truss elevation required to achieve a maximum damping ratio has been investigated through complex eigenvalue analysis,[4,5] and dynamic stiffness methods.[6] The performance of a damped-outrigger in reducing the seismic response was also verified experimentally.[8] Huang and Takeuchi[4] indicated that the optimal elevation of a damped-outrigger incorporating viscous dampers ranges from 50% to 80% of the building height. In addition, the seismic performance of multioutrigger was also investigated.[9] The damped-outrigger system adopting viscous dampers as energy dissipation device has been utilized in actual construction projects.[10] In addition, the outrigger truss member, incorporating buckling-restrained brace (BRB),[11] was utilized to limit the maximum forces generated in columns, at connections, and in core walls in recent design practices.[12]

In this study, the BRB is incorporated as an energy dissipation device in the damped-outrigger (BRB-outrigger) system, as shown in Figure 2. The BRBs are arranged vertically between the outrigger truss ends and the perimeter columns. The outrigger truss, BRB, and the perimeter column below the outrigger elevation act in series. Therefore, the maximum force demands in the outrigger truss members and perimeter columns are limited by BRB's axial force capacity. This provides engineers with clear force demands when designing the perimeter columns and outrigger truss members. As shown in Figure 2, when the building deforms toward the right, the right BRB is in compression, and the left in tension. As the BRB's axial deformation exceeds its yield deformation ($u_{d,y}$) as expected during large earthquakes, the BRB dissipates energy through its inelastic deformation, thereby reducing building seismic responses. The stable BRB hysteresis response provides the system with a stable energy dissipation mechanism. During minor earthquakes, a properly designed BRB-outrigger system can behave like a traditional elastic outrigger through BRB's elastic responses. In addition, the feasible BRB strength and stiffness are suitable for various structural configurations.

When viscous dampers are adopted in damped-outrigger system to control responses induced from wind and seismic loads, the design requirements and velocity ranges corresponding to these two demands are usually different.[13] The wide axial force capacity range and feasible stiffness of BRB allows the BRB-outrigger system to be an alternative in resisting seismic loads. However, the wind loads are sometimes greater than seismic lateral loads for high-rise buildings. This could lead to very large axial force and stiffness demands on the BRB because it is inappropriate to allow BRBs to yield due to wind loads. In such circumstances, the BRB might be overdesigned and may not develop satisfactory hysteretic responses during large earthquakes. The combined usage of viscous dampers and BRB in resisting wind and seismic loads respectively could be further investigated in future. This study focuses on the performance of a single BRB-outrigger system in resisting seismic loads.

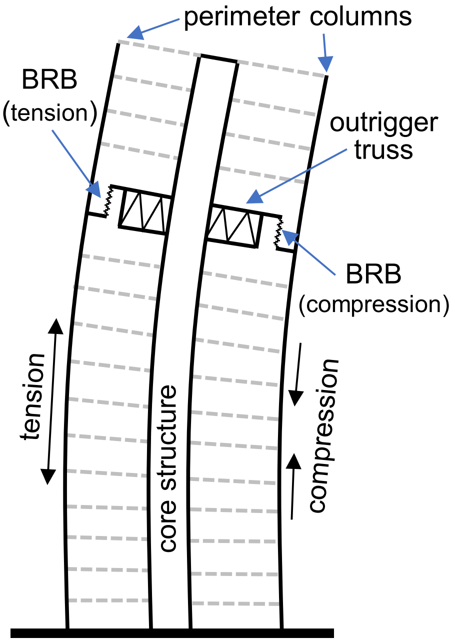

FIGURE 2 Buckling-restrained brace-outrigger system [Colour figure can be viewed at wileyonlinelibrary.com]

This study investigates the optimal outrigger elevation, optimal relationships between the outrigger truss flexural stiffness (k_t), BRB's axial stiffness (k_d) together with the yield roof drift ratio (θ_r), and perimeter column axial stiffness (k_c) to minimize the building seismic responses through spectral analysis (SA), incorporating the equivalent damping concept to consider the BRB's inelastic performance. A nonlinear response history analysis (NLRHA) was also performed to verify the effectiveness of the SA results. The reduction factors for reducing the maximum roof drift ratio and acceleration are adopted as the indicators in the parametric study. This study concludes with a design recommendation for a single BRB-outrigger system.

2 | ANALYTICAL MODELS

2.1 | Simplified structure

A core-tube type structure with a BRB-outrigger system is simplified as shown in Figure 3. For simplicity, it is assumed that the building's lateral stiffness is concentrated on the core structure. The core structure is represented by a cantilever column with uniformly distributed flexural rigidity EI. Each of the perimeter columns of height h has an axial stiffness k_c and a pinned support at the base. The outrigger trusses are located at a height αh above the ground. The outrigger trusses on both sides of the core structure are assumed identical to each other, and each has a flexural stiffness k_t. The connections between the outrigger trusses and the core structure have full moment-transfer capacity. The BRB is arranged vertically and connects the outrigger truss end (points G and E in Figure 3) to the perimeter column (points F and D in Figure 3). The axial stiffness of each BRB is k_d, and both ends of the BRB are free to rotate. The masses are assumed to be concentrated at the core structure and distributed uniformly along the height. The force and deformation relationship of the BRB is bilinear, with a postyield stiffness ratio p. The other members are assumed to be linearly elastic. The core structure rotation at the outrigger elevation (θ_1) can be expressed as follows:

$$\theta_1 = \frac{1}{l_t}(u_c + u_t + u_d) = \frac{1}{l_t}\left[1 + \frac{k_c}{\alpha}\left(\frac{1}{k_t} + \frac{1}{k_d}\right)\right]u_c = \frac{k_d}{l_t}\left(\frac{\alpha}{k_c} + \frac{1}{k_t} + \frac{1}{k_d}\right)u_d \tag{1}$$

where l_t is the outrigger truss span, u_d and u_c are the axial deformations of BRB and perimeter column below outrigger elevation, respectively, and u_t is the outrigger truss's flexural deformation. The vertical force acting at outrigger truss end (F), the corresponding moment applied at the core structure (M), and the equivalent rotational spring stiffness induced from outrigger system (k_g) can be calculated as follows:

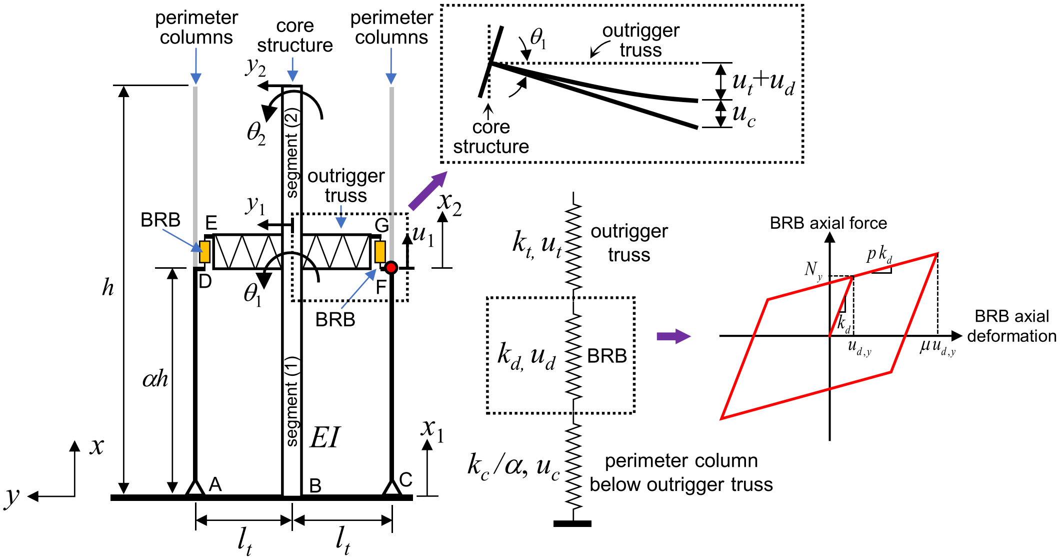

FIGURE 3 Simplified structure and force and deformation relationship of buckling-restrained brace [Colour figure can be viewed at wileyonlinelibrary.com]

$$F = \frac{u_c k_c}{\alpha} = k_d u_d = k_t u_t \tag{2}$$

$$M = 2Fl_t = \frac{2l_t^2}{\alpha/k_c + 1/k_d + 1/k_t}\theta_1 = \frac{2l_t^2}{1/k_b + 1/k_d}\theta_1 = k_g\theta_1, \quad \text{where} \quad k_b = \frac{1}{\alpha/k_c + 1/k_t} \tag{3}$$

The BRB-outrigger system can be further simplified as a rotational spring with stiffness k_g, attached to the core structure, as shown in Figure 4A. The core structure below and above outrigger elevation is divided into segments (1) and (2), respectively. The lateral displacement, y_N (x_N, t), at distance x_N from the bottom end of each segment, at time t, can be solved by applying the D'Alembert principle:

$$EI\frac{\partial^4 y_N(x_N,t)}{\partial x_N^4} + m\frac{\partial^2 y_N(x_N,t)}{\partial t^2} = 0, \qquad N = 1 \text{ or } 2 \tag{4}$$

where m is the mass per unit height. It is assumed that the lateral displacements within segments (1) and (2) (y_1 and y_2) are in the form as follows:

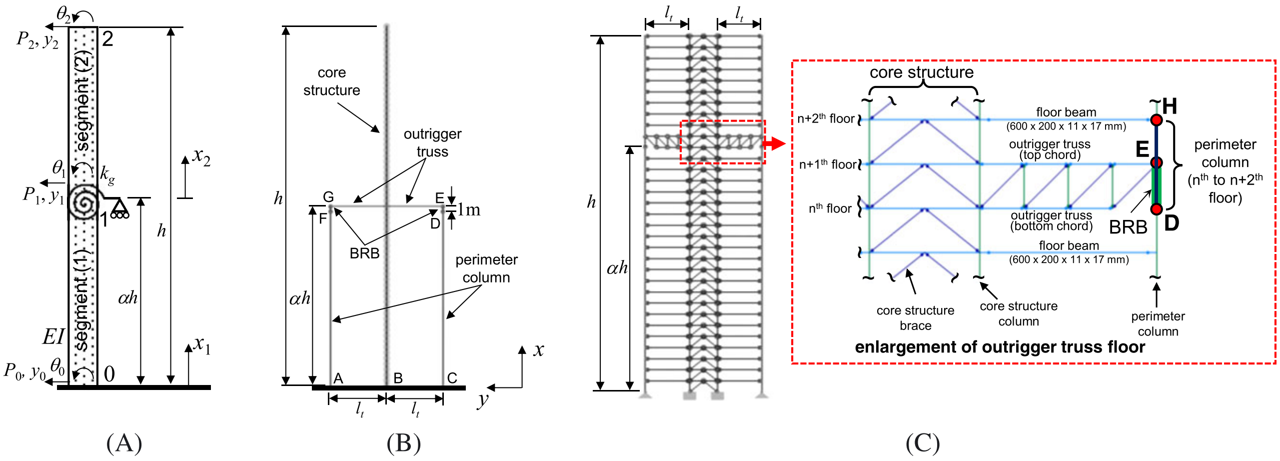

FIGURE 4 Schematic views A, uniform mass, B, discrete mass, and C, member-by-member models [Colour figure can be viewed at wileyonlinelibrary.com]

$$y_N(x_N, t) = Y_N(x_N)Q(t), \qquad N = 1 \text{ or } 2 \tag{5}$$

Substituting Equation 5 into Equation 4, the solution of lateral displacement is as follows:

$$Y_N(x_N) = A_{N1}\cosh\left(\frac{\lambda}{h}x_N\right) + A_{N2}\sinh\left(\frac{\lambda}{h}x_N\right) + A_{N3}\cos\left(\frac{\lambda}{h}x_N\right) + A_{N4}\sin\left(\frac{\lambda}{h}x_N\right), \ \text{ where } \lambda^4 = \frac{m\omega^2h^4}{EI} \tag{6}$$

where ω is the angular frequency. By applying the boundary conditions at the ends of segments (1) and (2), Equation 6 can be expressed in matrix form as follows:

$$\mathbf{u}_N = \begin{bmatrix} y_{N-1} \\ \theta_{N-1}h \\ y_N \\ \theta_N h \end{bmatrix} = \begin{bmatrix} Y_N(0) \\ Y_N'(0)h \\ Y_N(L_N) \\ Y_N'(L_N)h \end{bmatrix} = \begin{bmatrix} 1 & 0 & 1 & 0 \\ 0 & \lambda & 0 & \lambda \\ C_N & S_N & c_N & s_N \\ \lambda S_N & \lambda C_N & -\lambda s_N & \lambda c_N \end{bmatrix} \begin{bmatrix} A_{N1} \\ A_{N2} \\ A_{N3} \\ A_{N4} \end{bmatrix} = \mathbf{D}_N\mathbf{A}_N, \quad N = 1 \ \text{ or } \ 2, \tag{7}$$

$$\text{where} \quad \begin{matrix} L_1 = \alpha h \\ L_2 = (1-\alpha)h \\ Y_N' = \dfrac{dY_N(x)}{dx} \end{matrix} \quad \begin{matrix} C_1 = \cosh(\alpha\lambda) & C_2 = \cosh(\lambda-\alpha\lambda) \\ S_1 = \sinh(\alpha\lambda) & S_2 = \sinh(\lambda-\alpha\lambda) \\ c_1 = \cos(\alpha\lambda) & c_2 = \cos(\lambda-\alpha\lambda) \\ s_1 = \sin(\alpha\lambda) & s_2 = \sin(\lambda-\alpha\lambda) \end{matrix}$$

where $\mathbf{u_1}$ and $\mathbf{u_2}$ are the displacement matrices corresponding to both ends of segments (1) and (2), respectively. As shown in Figure 4A, for individual segment N, the bottom and top ends' shear (${}_{(N)}P_{N\text{-}1}$, ${}_{(N)}P_N$) and bending moments (${}_{(N)}M_{N\text{-}1}$, ${}_{(N)}M_N$) are expressed in matrix $\mathbf{P_N}$ as follows:

$$\begin{aligned} \mathbf{P}_N = \begin{bmatrix} {}_{(N)}P_{N-1} \\ {}_{(N)}M_{N-1}/h \\ {}_{(N)}P_N \\ {}_{(N)}M_N/h \end{bmatrix} &= \frac{EI}{h^3}\begin{bmatrix} 0 & \lambda^3 & 0 & -\lambda^3 \\ -\lambda^2 & 0 & \lambda^2 & 0 \\ -\lambda^3 S_N & -\lambda^3 C_N & -\lambda^3 s_N & \lambda^3 c_N \\ \lambda^2 C_N & \lambda^2 S_N & -\lambda^2 c_N & -\lambda^2 s_N \end{bmatrix}\mathbf{A}_N \\ &= \frac{EI}{h^3}\begin{bmatrix} 0 & \lambda^3 & 0 & -\lambda^3 \\ -\lambda^2 & 0 & \lambda^2 & 0 \\ -\lambda^3 S_N & -\lambda^3 C_N & -\lambda^3 s_N & \lambda^3 c_N \\ \lambda^2 C_N & \lambda^2 S_N & -\lambda^2 c_N & -\lambda^2 s_N \end{bmatrix}\mathbf{D}_N^{-1}\mathbf{u}_N = \mathbf{B}_N\mathbf{u}_N \end{aligned} \tag{8}$$

Incorporating the rotational spring (k_g) and the degree of freedom at points 1 and 2 (Figure 4A), the force and displacement relationship of the system can be expressed as follows:

$$\begin{bmatrix} P_1 \\ M_1/h \\ P_2 \\ M_2/h \end{bmatrix} = \frac{EI}{h^3}\begin{bmatrix} \dfrac{(S_1c_1 + C_1s_1)\lambda^3}{1-C_1c_1} + \dfrac{(S_2c_2 + C_2s_2)\lambda^3}{1-C_2c_2} & \dfrac{-\lambda^2S_1s_1}{1-C_1c_1} + \dfrac{\lambda^2S_2s_2}{1-C_2c_2} & \dfrac{-(S_2 + s_2)\lambda^3}{1-C_2c_2} & \dfrac{(C_2-c_2)\lambda^2}{1-C_2c_2} \\ \dfrac{-\lambda^2S_1s_1}{1-C_1c_1} + \dfrac{\lambda^2S_2s_2}{1-C_2c_2} & \dfrac{\lambda(C_1s_1-S_1c_1)}{1-C_1c_1} + \dfrac{\lambda(C_2s_2-S_2c_2)}{1-C_2c_2} + \dfrac{h}{EI}k_g & \dfrac{(c_2-C_2)\lambda^2}{1-C_2c_2} & \dfrac{\lambda(S_2-s_2)}{1-C_2c_2} \\ \dfrac{-(S_2 + s_2)\lambda^3}{1-C_2c_2} & \dfrac{\lambda^2(c_2-C_2)}{1-C_2c_2} & \dfrac{(S_2c_2 + C_2s_2)\lambda^3}{1-C_2c_2} & \dfrac{-\lambda^2S_2s_2}{1-C_2c_2} \\ \dfrac{(C_2-c_2)\lambda^2}{1-C_2c_2} & \dfrac{\lambda(S_2-s_2)}{1-C_2c_2} & \dfrac{-\lambda^2S_2s_2}{1-C_2c_2} & \dfrac{\lambda(C_2s_2-S_2c_2)}{1-C_2c_2} \end{bmatrix}\begin{bmatrix} y_1 \\ \theta_1h \\ y_2 \\ \theta_2h \end{bmatrix} = \mathbf{Bu} \tag{9}$$

Matrix $\mathbf{B}$ expresses the relationships between force and displacement of the core structure's dynamic responses including the outrigger effect. Thus, λ, ω, and the associated vibration periods of the nth mode can be obtained by solving $\det \mathbf{B} = 0$. The nth mode shape can be obtained by substituting λ into Equations 6 and 7. In this study, the simplified structure shown in Figure 4A is known as uniform mass (UM) model and is used when performing SA. Figure 4B shows the analytical model with discrete mass (DM) distribution along the height of the core structure, when performing NLRHA. Figure 4C shows the refined member-by-member (MBM) model used for verifying the effectiveness of UM and DM models. The details of DM and MBM models will be introduced in the following sections.

2.2 | Modal analysis

As 4 degrees of freedom are considered in the UM model (y_1, θ_1, y_2, and θ_2 as shown in Figure 4A), the first 4 modes are considered while performing SA. The SA is performed by using the modal analysis results. It is assumed that the mode shapes remain the same and the modal superposition principle is applicable when the BRBs deform inelastically.[14] If $\phi_r(x)$ is the rth mode shape, the core structure's lateral displacement $y(x, t)$ can be expressed by modal superposition as follows:

$$y(x,t)=\sum_{r=1}^{4}\phi_r(x)Q_r(t) \tag{10}$$

Substitute Equation 10 into Equation 4, the following can be obtained:

$$m\sum_{r=1}^{4}\phi_r(x)\ddot{Q}_r(t)+EI\sum_{r=1}^{4}\phi_r^{''''}(x)Q_r(t)=0,\quad \text{where } \phi_r^{''''}(x)=\frac{d^4\phi_r(x)}{dx^4} \text{ and } \ddot{Q}_r(t)=\frac{d^2Q_r(t)}{dt^2} \tag{11}$$

Applying modal orthogonality and integrating with respect to x from 0 to h, Equation 11 becomes

$$\ddot{Q}_n(t)\int_0^h m[\phi_n(x)]^2dx+Q_n(t)\int_0^h EI\phi_n(x)\phi_n^{''''}(x)dx=0 \tag{12}$$

The modal mass (M_n), modal stiffness (K_n), and elastic vibration period (T_n) are calculated as follows:

$$M_n=\int_0^h m[\phi_n(x)]^2dx,\qquad K_n=\int_0^h EI\phi_n(x)\phi_n^{''''}(x)\ dx,\qquad T_n=2\pi\sqrt{\frac{M_n}{K_n}},\qquad \text{where } \phi_n^{''''}(x)=\frac{d^4\phi_n(x)}{dx^4} \tag{13}$$

The detailed SA procedure will be introduced in the following sections.

2.3 | Parameter definitions

As shown in Figure 3, the performance of outrigger is affected by k_t, k_d, k_c, and the outrigger elevation α. For the purpose of parametric study, 4 dimensionless parameters (S_{bc}, R_{dt}, R_{dc}, and R_{db}) are defined to represent the structure's properties. The outrigger stiffness parameter (S_{bc}) is adopted to indicate the magnitude of how outrigger affects the structure and is defined by the ratio of rotational stiffness of outrigger ($k_b l_t^2$) when k_d is infinite to the core structure's rotational stiffness (EI/h). S_{bc} can be computed as follows:

$$S_{bc}=\frac{k_b l_t^2}{EI/h}=\frac{l_t^2 h}{EI(1/k_t+\alpha/k_c)} \tag{14}$$

A larger S_{bc} value indicates a more significant outrigger effect. A longer outrigger truss span (l_t) while k_b remains constant, or a stiffer outrigger truss (greater k_t), or a stiffer perimeter column (greater k_c) can enhance the outrigger effect. However, when EI, h, l_t, k_t, and k_c are kept constant while increasing α, the outrigger effect would be smaller. For taller structures, EI/h would be larger because of greater seismic lateral force demands. Thus, in this study, smaller S_{bc} value is adopted to represent taller structures. In addition to S_{bc}, the ratio of BRB axial stiffness to outrigger truss's flexural stiffness (R_{dt}) and the BRB stiffness parameters (R_{db}, R_{dc}) are defined as follows:

$$R_{dt}=\frac{k_d}{k_t},\quad R_{dc}=\frac{k_d}{k_c},\quad R_{db}=\frac{k_d}{k_b}=k_d\left(\frac{1}{k_t}+\frac{\alpha}{k_c}\right)=R_{dt}+\alpha R_{dc} \tag{15}$$

In the design practice, the perimeter column sizes are usually determined by gravity load demands; thus, it is possible that BRB has to be designed based on perimeter column sizes. The R_{dc} describes the stiffness relationship between

BRB and the perimeter column, and R_{db} describes the relationship between BRB and the combination of perimeter column and outrigger truss. The larger R_{db} or R_{dc} value indicates the BRB is stiffer. The optimal R_{db} or R_{dc} value could provide an easy and straightforward way for engineers to roughly design BRB in the preliminary design stage. In addition, a smaller R_{dt} value should be preferred because it results in larger BRB axial deformation demand.

For each set of analyses, α varies from 0 to 1 under given k_c, k_d, and k_t. As indicated in Equation 3, k_g decreases with increasing α when k_t, k_d, and k_c are kept as constant. Two methods were developed for the parametric study. Method I (Met. I) sets k_b and k_g as constants while changing α under a given R_{db} in each analysis set. As indicated in Equation 3, k_b is kept constant by fixing both k_t and k_c/α. Thus, k_c is proportional to α. This suggests that k_c increases with increasing α in Met. I. Method II (Met. II) sets k_c as a constant by specifying R_{dc} in each analysis set. Thus, k_g decreases with increasing α. Met. I provides a straightforward analysis procedure because only α is changed, while Met. II would be more realistic for practical design purpose because k_c and α are set to be independent to each other. Table 1 summarizes the variation of parameters in each analysis set when α varies from 0 to 1 in Met. I and Met. II.

The BRB axial yield deformation ($u_{d,y}$) is crucial as it determines the start of energy dissipation. From Equation 1, $u_{d,y}$ and the corresponding core structure rotation at outrigger elevation when BRB yields (θ_y) can be expressed as follows:

$$\theta_y = \frac{k_d}{l_t}\left(\frac{\alpha}{k_c} + \frac{1}{k_t} + \frac{1}{k_d}\right)u_{d,y} = \frac{1}{l_t}(\alpha R_{dc} + R_{dt} + 1)u_{d,y} = \frac{1}{l_t}(R_{db} + 1)u_{d,y} \tag{16}$$

In this study, when the roof drift ratio in the first mode shape reaches a given yield drift ratio (θ_r), the corresponding BRB axial deformation is referred to as $u_{d,y}$. θ_r should be properly selected so that $u_{d,y}$ lies in a reasonable range based on the actual BRB configuration. The investigation on relationship between θ_r and $u_{d,y}$, and its effects on the seismic performance, will be presented in the following sections.

2.4 | Numerical models

To perform NLRHA by using OpenSees,[15] the DM model (Figure 4B) was developed. The core structure, BRBs, and the perimeter columns are all included in the DM model. The masses are concentrated at the nodes that are uniformly distributed along the core structure height with an equal spacing of either 1 m (DM1) or 4 m (DM4). Each of the outrigger trusses is modeled as a beam element with a flexural stiffness k_t. The core structure, outrigger truss, and perimeter columns are modeled by using the Elastic Beam Column element.[16] The BRBs are modeled as truss elements, with a fixed length of 1 m. The bottom end of the core structure (point B in Figure 4B) is fixed, and the bottom ends of perimeter columns (points A and C in Figure 4B) are free to rotate about the z-axis. The 2 ends of the BRBs are free to move in the x-direction and free to rotate about the z-axis.

Figure 4C shows the MBM model that was analyzed by using the PISA3D program.[17] The details of story levels, core structure, outrigger truss, and floor beams are included in the MBM model. The analytical results of MBM model were used to compare with the results of UM, DM1, and DM4 models, to verify the effectiveness of those simplified models. The beams and columns of MBM model are modeled by using the beam column elements,[17] the braces and outrigger truss members are modeled as truss elements. Each story is 4 m high, the mass at each floor level is concentrated at the midspan of beam of core structure. The core structure is represented by a braced frame with a lateral stiffness close to EI. The bottom end of the perimeter columns is pinned. Figure 4C also shows enlarged details of the outrigger truss. The outrigger truss's top and bottom chords are located at the nth + 1 and nth floors, respectively. The BRB's upper and lower ends connect to the outrigger's top chord end (point E) and to the perimeter column at the nth floor, respectively. No rigid diaphragm was assigned in the MBM model.

Figure 5 shows the elevations and floor framing plan of the outrigger floor. It is assumed that the core structure provides sufficient lateral force resistance in horizontal directions, so that the core structure remains elastic. The outrigger truss span (l_t) is 16 m, and the building heights (h) are 64, 128, and 256 m for the 16, 32, and 64-story models, respectively. Each floor area is 2184 m^2 (52 m × 42 m), with a uniformly distributed dead load of 0.8 tonf/m^2, including the

TABLE 1 Parameter variations while α increases from 0 to 1 in each analysis set in Met. I and Met. II

	S_{bc}	k_g	k_b	k_t	k_c	k_d
Met. I	Fixed	Fixed	Fixed	Fixed	Increased	Fixed
Met. II	Decreased	Decreased	Decreased	Fixed	Fixed	Fixed

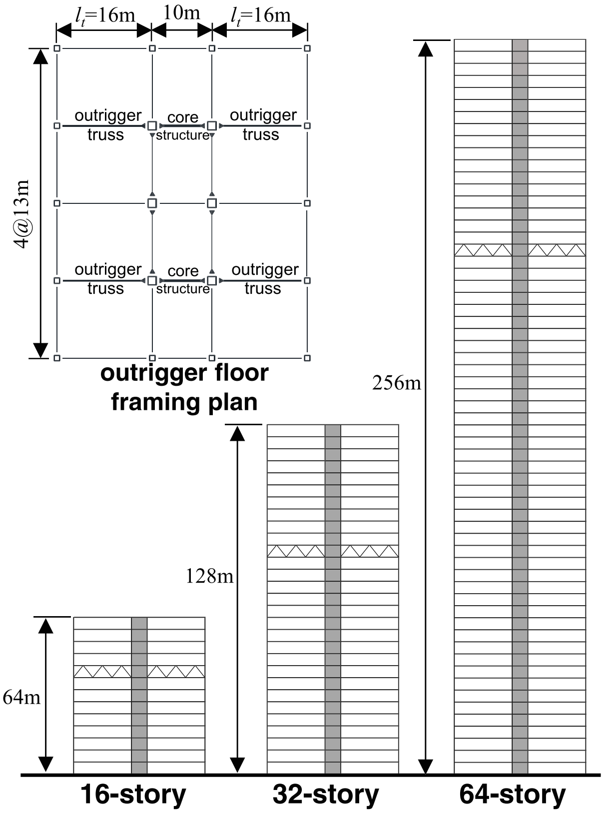

FIGURE 5 Elevation and outrigger floor framing plan of analytical models

member self-weight. The mass is 900 ton on each floor of the MBM models, 225 and 900 ton concentrated at each node on the core structure of the DM1 and DM4 model, respectively, and 225 ton/m uniformly distributed along the core structure height for the UM model. For simplicity, the force and deformation relationships are bilinear for BRBs and linearly elastic for all the other members in UM, DM1, DM4, and MBM models. The secondary effects due to gravity loads are excluded. Table 2 shows h, EI, and the ranges of R_{db} for Met. I and R_{dc} range for Met. II. EI is determined by setting the fundamental mode vibration period to be approximately 0.03 h. S_{bc} is set to be 3.03, 1.38, and 0.66 for the 16, 32, and 64-story models in the Met. I analysis, respectively. In Met. II, S_{bc} varies with changing α but is set to be 3.03, 1.38, and 0.66 for the 16, 32, and 64-story models, respectively, when α equals 0.7. The relationships between S_{bc} and α for Met. I and Met. II are shown in Figure 6A. Figure 6B shows the relationship between α and the corresponding R_{dc} under given R_{db} values for Met. I. Figure 6C shows the relationship between α and the corresponding R_{db} under given R_{dc} values for Met. II. Figure 6D shows the relationship between k_g and α for the 32-story model.

2.5 | Comparison between UM, DM1, DM4, and MBM models

The modal analysis and NLRHA results of MBM model were used to verify the effectiveness of UM (used for performing SA), DM1 (used for performing NLRHA), and DM4 models. In addition, the analyses on MBM models without outrigger (core structure only) and with the elastic outrigger (by setting $u_{d,y}$ to be infinity) were performed to demonstrate the prominent performance of BRB-outrigger system. The 32-story model (S_{bc} = 1.38) with α = 0.7, R_{dt} = 0.1, R_{dc} = 5.0,

TABLE 2 Parameters of analytical models for Met. I and Met. II analyses

			Met. I		Met. II
Model	***h*** **(m)**	***EI*** **(kN-m^2)**	R_{db}	S_{bc}	R_{dc}
16-story	64	4.1×10^9	0.15-20.0	3.03	0.1-20.0
32-story	128	1.6×10^{10}	0.15-20.0	1.38	0.1-20.0
64-story	256	6.5×10^{10}	0.15-20.0	0.66	0.1-20.0

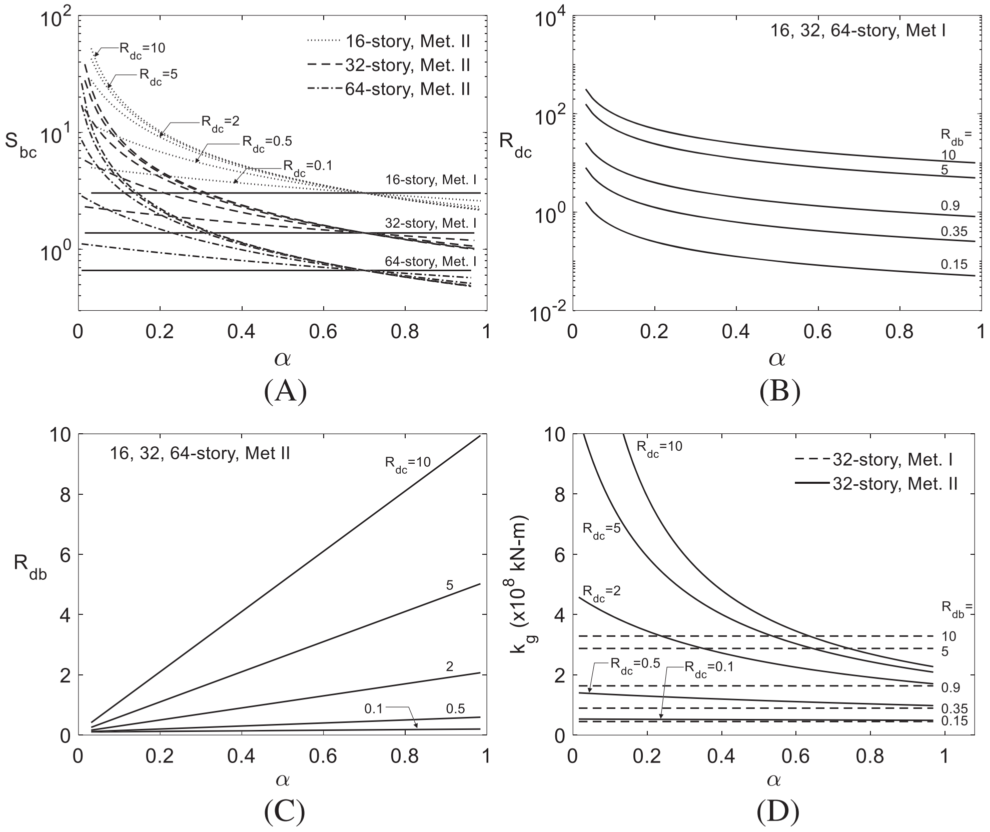

(A) (B)

(C) (D)

FIGURE 6 Relationships between A, S_{bc}, B, R_{dc}, C, R_{db}, and D, k_g with α

and $\theta_r = 1/750$ was chosen as the example model. Table 3 shows the member sizes and material properties. The perimeter columns were designed according to the axial force demand in the first story (0.8 tonf × 104 m^2 [tributary area] × 32 stories + 1.1 × 1.3 × N_y), where N_y is the BRB core yield force capacity and 1.1 and 1.3 are factors of overstrength and strain hardening, respectively.[18,19] According to the member sizes, k_c, k_d, and k_t are 0.486 × 10^6, 2.43 × 10^6, and 24.3 × 10^6 kN/m, respectively. $u_{d,y}$ is 5.2 mm, and N_y (=$k_d \times u_{d,y}$) is 12368 kN. Thus, the perimeter column axial force demand in the first story (44190 kN) can be calculated. Considering a strength reduction factor of 0.9,[20] the axial force demand-to-capacity ratio of the perimeter column is 0.47.

Table 4 and Figure 7 show the vibration periods and mode shapes of the first 4 modes. The vibration periods of UM and DM1 models are close to each other. This suggests that the DM1 model developed in OpenSees with mass spacing of 1 m is a good representation of the UM model. As the masses are concentrated at nodes with 4-m spacing in MBM and DM4 model, the vibration periods are longer if compared with UM and DM1 models. In addition, there are vibration period differences between DM4 and MBM models because the core structure span of 10 m was not included in the DM4 model, and the behavior of the braced frame to represent core structure in MBM model may not accurately resemble a cantilever column. Table 4 also shows the vibration periods of the MBM model when the BRBs remain elastic (elastic-outrigger) and also without outrigger (no outrigger). The much longer first to fourth mode vibration periods of MBM (no outrigger) as compared with MBM with outrigger system show significant outrigger effect. In addition, NLRHA on the aforementioned analytical models was also performed. Table 5 shows the information of 8 ground motions adopted for NLRHA. Figure 8A and B shows the 2% damping response spectra of the original observed and

TABLE 3 32-story MBM model member sizes ($\alpha = 0.7$, $R_{dt} = 0.1$, $R_{dc} = 5.0$, $\theta_r = 1/750$)

Member	Size	Material Property
Perimeter column	Box 1 000 × 1 000 × 85 mm	Linearly elastic (SN490)
BRB	+775 × 32 mm (cross-sectional area = 48 576 mm^2)	Bilinear (SN490, yield stress = 345 MPa, p = 0.01)

TABLE 4 The modal analysis results of the example UM, DM1, DM4, and MBM models

	Vibration Period (s)			
Model	**First Mode**	**Second Mode**	**Third Mode**	**Fourth Mode**
UM	2.498	0.512	0.198	0.100
DM1	2.498	0.515	0.199	0.100
DM4	2.540	0.529	0.204	0.102
MBM MBM (elastic-outrigger)	2.587	0.581	0.253	0.142
MBM (no outrigger)	3.770	0.646	0.253	0.145

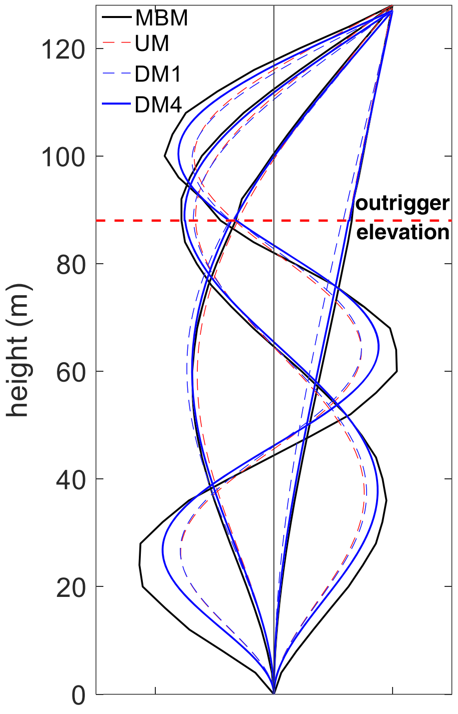

FIGURE 7 The first to the fourth mode shapes of uniform mass, discrete mass (1-m mass spacing), discrete mass (4-m mass spacing, and member-by-member 32-story models [Colour figure can be viewed at wileyonlinelibrary.com]

TABLE 5 The ground motions used for NLRHA

Ground Motion	Earthquake Event	Date	Magnitude	Depth (km)	PGA (gal)	Scale Factor
Tohoku	Miyagi	June 12, 1978	*M*7.7	44	258	2.03
El Centro	El Centro	May 18, 1940	*M*6.9	16	342	2.54
Taft	Kern Country	July 21, 1952	*M*7.3	16	176	4.90
Kumamoto	Kumamoto	April 16, 2016	*M*7.0	10	627	1.82
KobeJMA	Great Hanshin	January 17, 1995	*M*6.9	18	821	1.19
Sendai	Tohoku	March 11, 2011	*M*9.0	29	1517	1.33
ChiChi	ChiChi	September 21, 1999	*M*7.3	33	439	0.66
BCJ-L2	Artificial	—	—	—	356	1.14

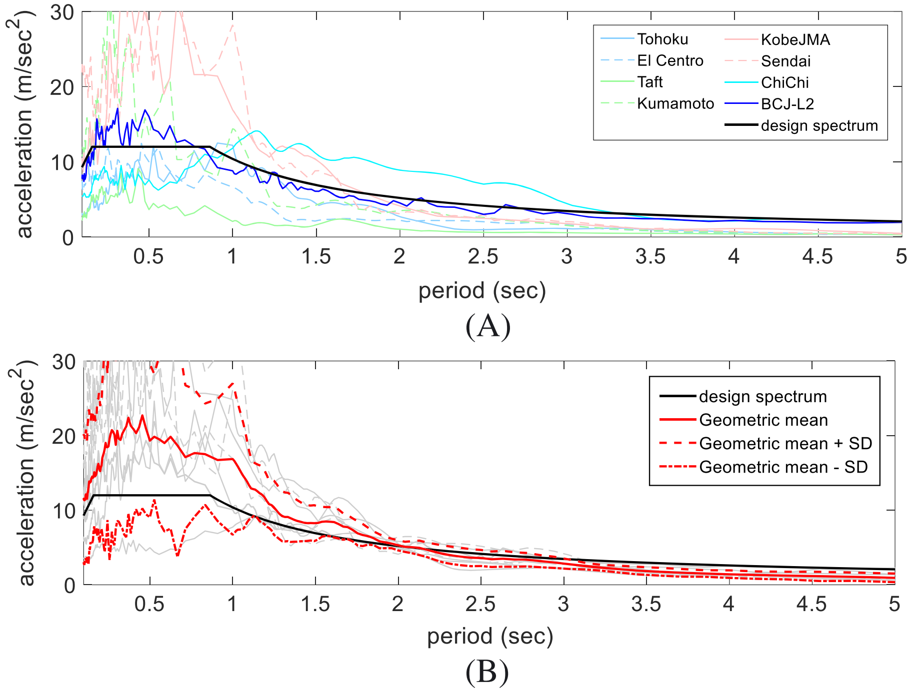

(A)

(B)

FIGURE 8 The response spectra of the A, original observed and B, scaled ground motions and design spectrum [Colour figure can be viewed at wileyonlinelibrary.com]

scaled ground motions. The response spectra of the original observed ground motions were scaled to fit the design spectral acceleration within the range of $0.2T_1$ to $1.5T_1$, where T_1 is the first mode period (2.5 s). Rayleigh damping of 0.02 for the first and second modes was adopted for all NLRHA. In this study, the maximum roof drift ratio ($\theta_{\max}$) and the

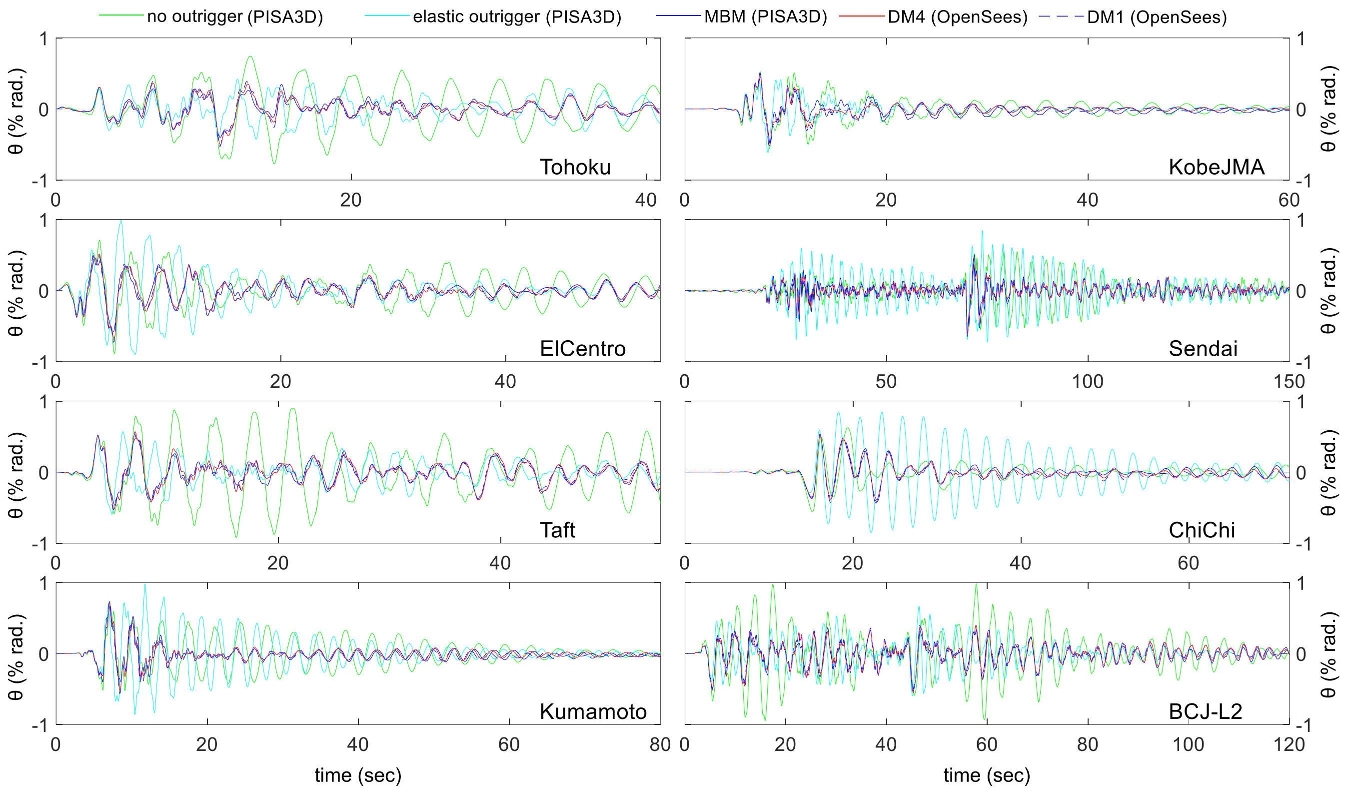

FIGURE 9 The nonlinear response history analysis results of roof displacement histories of the 32-story model under each ground motion [Colour figure can be viewed at wileyonlinelibrary.com]

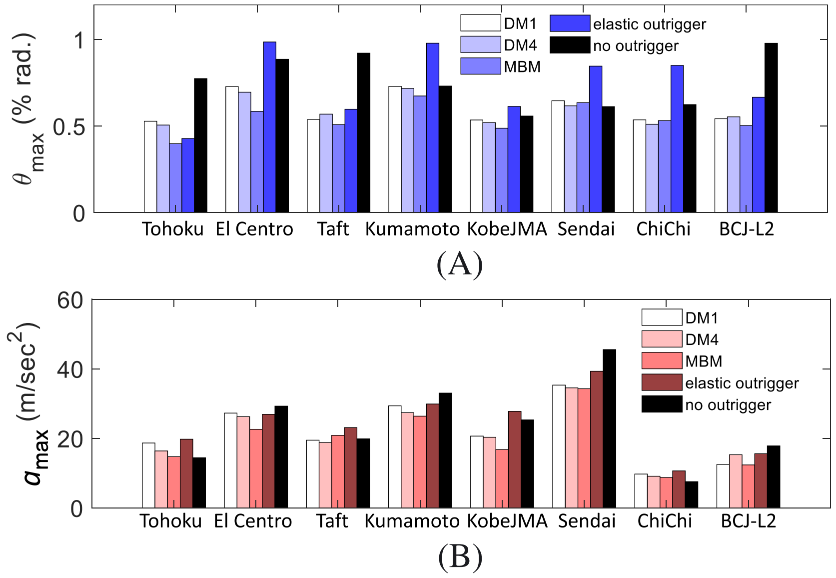

(A)

(B)

FIGURE 10 The A, $\theta_{\max}$ and B, $a_{\max}$ responses from nonlinear response history analysis results [Colour figure can be viewed at wileyonlinelibrary.com]

maximum roof acceleration response ($a_{\max}$) are assigned as measures of seismic performance. Figures 9 and 10 show the roof drift histories, the $\theta_{\max}$ and $a_{\max}$ under each NLRHA. If the cases without outrigger, with elastic outrigger, and with BRB-outrigger are compared, the elastic outrigger reduces the displacement responses only in some cases, but the peak accelerations are greater than the BRB-outrigger cases (DM1, DM4, and MBM). Figure 9 shows close trends and marginal differences among DM1, DM4, and MBM models. Although the peak responses among DM1, DM4, and MBM models are slightly different, this may not affect the parametric analysis in investigating optimal parameters. Thus, the DM1 model is used when performing NLRHA using OpenSees for verifying the SA results. For simplicity, the BCJ-L2, which best matches the design spectrum, was adopted for NLRHA in the following sections.

3 | ANALYSIS PROCEDURES

To investigate the effects of α on the seismic performance and study the relationships among k_d, k_c, and k_t, the SA and NLRHA were performed. The analysis procedures are described in the following sections.

3.1 | Parameter computation in each analysis set

In each analysis set, when α varies from 0 to 1, Met. I sets R_{db} as a constant with respect to α and Met. II sets R_{dc} as a constant. In Met. I, the first step is to calculate k_b according to the given h, S_{bc}, and l_t. k_d can then be calculated from the given R_{db} in each analysis set. Finally, k_t and k_c are calculated from the given R_{dt}. In Met. II, k_d, k_c, and k_t are calculated by solving the simultaneous equations (Equations 14 and 15) with the given R_{dc} and R_{dt} and setting α to 0.7 in Equation 15.

3.2 | Spectral analysis

The SA is used to evaluate $\theta_{\max}$. The response of each mode is calculated separately, and then superposed by using the square root of the sum of the squares rule. For the nth mode response, as shown in Equation 16, when the core structure rotation at outrigger elevation reaches θ_y, the BRB initially yields, and the corresponding roof displacement is adopted as the yield roof displacement ($y_{\mathrm{top},n}$). In this study, θ_y is computed from the first mode shape when the roof drift reaches θ_r. When the BRB deforms inelastically, the postyield modal stiffness $K_n^{'}$ of nth mode can be computed as follows:

$$K_n^{'} = \left(\frac{T_n}{T_n^{'}}\right)^2 K_n = p_n K_n \tag{17}$$

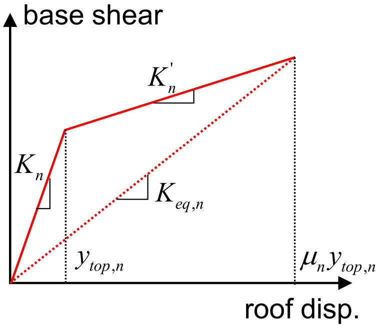

FIGURE 11 Relationship among K_n, K_n', and $K_{\mathrm{eq},n}$ [Colour figure can be viewed at wileyonlinelibrary.com]

where T_n' is the nth mode vibration period of the system after BRB has yielded and the k_d has been replaced by postyield stiffness (pk_d). If $y_{\max,n}$ is the maximum roof displacement and μ_n ($=y_{\max,n}/y_{\mathrm{top},n}$) is the ductility ratio in the nth mode, the equivalent stiffness ($K_{\mathrm{eq},n}$), the equivalent vibration period ($T_{\mathrm{eq},n}$), and the equivalent damping ratio ($h_{\mathrm{eq},n}$) can be calculated as follows[19,21,22]:

$$K_{\mathrm{eq},n}=K_n'+\frac{K_n-K_n'}{\mu_n},\quad T_{\mathrm{eq},n}=T_n\sqrt{\frac{K_n}{K_{\mathrm{eq},n}}},\quad h_{\mathrm{eq},n}=h_0+\frac{2}{\pi p_n\mu_n}\ln\left(\frac{1-p_n+p_n\mu_n}{\mu_n{}^{p_n}}\right),\quad \mu_n\geq 1 \tag{18}$$

where h_0 (0.02) is the inherent damping ratio. The relationships among K_n, K_n', and $K_{\mathrm{eq},n}$ are shown in Figure 11. If S_{pv} (T, h_0) is the pseudo velocity spectrum with vibration period T and damping ratio h_0, and $D_{h,n}$ is the reduction factor for computing S_{pv} (T, $h_{\mathrm{eq},n}$) because of the increased damping ratio ($h_{\mathrm{eq},n}$), the relationship between S_{pv} (T, h_0) and S_{pv} (T, $h_{\mathrm{eq},n}$) can be expressed as follows[21]:

$$S_{pv}\left(T,h_{\mathrm{eq},n}\right)=D_{h,n}S_{pv}(T,h_0),\qquad \text{where}\ \ D_{h,n}=\sqrt{\frac{1+\gamma h_0}{1+\gamma h_{\mathrm{eq},n}}},\ \ \gamma=75\ \ \text{for artifical waves} \tag{19}$$

The displacement response after the yielding of BRB (S_d ($T_{eq,n}$, $h_{eq,n}$)) is

$$S_d\left(T_{\mathrm{eq},n},\ \ h_{\mathrm{eq},n}\right)=\frac{T_{\mathrm{eq},n}}{2\pi}D_{h,n}S_{pv}\left(T_{\mathrm{eq},n},\ \ h_0\right) \tag{20}$$

The maximum displacement of each mode is calculated by an iterative process. The first step is to obtain the maximum roof displacement (S_d (T_n, h_0)) by using the elastic vibration period (T_n) and inherent damping ratio. Then, calculate the corresponding ductility ratio (S_d (T_n, h_0)/$y_{\mathrm{top},n}$) and the equivalent damping ratio $h_{\mathrm{eq},n}$ (Equation 18). The updated displacement because of increased damping ratio and the equivalent vibration period (S_d ($T_{\mathrm{eq},n}$, $h_{\mathrm{eq},n}$)) is computed by Equation 20. The iterations should be performed until the displacements, before and after being updated, are satisfactorily close. Table 6 shows the SA results of the example model in Section 2.4. The first mode dominates the response, and only slight inelastic response in the second mode response. The $\theta_{\max}$ computed from SA by using square root of the sum of the squares is 0.588% rad., and the average $\theta_{\max}$ obtained from NLRHA described in section 2.5 are 0.560%, 0.586%, and 0.541% rad. for the DM1, DM4, and MBM models, respectively.

TABLE 6 SA results of example model

	Mass Participation Ratio	**Yield Roof Drift Ratio ($y_{\mathrm{top},n}/h$, % rad.)**	**$\theta_{\max}$ (% rad.)**	**μ_n**	**$h_{\mathrm{eq},n}$**
First mode	72.6%	0.133	0.586	4.41	0.085
Second mode	16.5%	0.052	0.052	1.02	0.020
Third mode	7.2%	0.281	0.005	0.02	0.020
Fourth mode	3.7%	0.021	0.001	0.05	0.020

3.3 | Nonlinear response history analysis

The results of NLRHA using BCJ-L2 ground motion are used to verify the SA results. In this study, OpenSees was utilized to perform NLRHA by using the DM1 models. The elastic design acceleration spectrum used by SA and the BCJ-L2 acceleration spectrum are shown in Figure 8A. In each analysis, the BCJ-L2 acceleration spectrum was scaled according to the S_a (T_1) method,[23] so that the spectral acceleration at the linearly elastic fundamental period of DM1 model matches the target design spectrum.

4 | ANALYSIS RESULTS

4.1 | Investigation of θ_r and R_{dt}

Prior to investigating the optimal values of α, R_{db}, and R_{dc} to minimize the building's seismic response, the effects of θ_r and R_{dt} on the analytical results have been studied. θ_r controls the BRB performance. A larger θ_r suggests that the BRB starts dissipating energy at a relative large roof drift ratio and thus may reduce the BRB's energy dissipation efficiency. However, if θ_r is too small, the BRB may yield in a minor earthquake or use up its ductility capacity during a large earthquake. Smaller R_{dt} indicates that the outrigger truss is stiffer than BRB and would result in a larger $u_{d,y}$ and vice versa. In this section, 2 sets of analyses are performed. The first set of analyses was performed by fixing $R_{dt} = 0.1$, $R_{db} = 3.5$ (Met. I), and $R_{dc} = 5.0$ (Met. II) but varying θ_r between 1/50 and 1/950. In the second set of analyses, θ_r is fixed at 1/750, and the other parameters are the

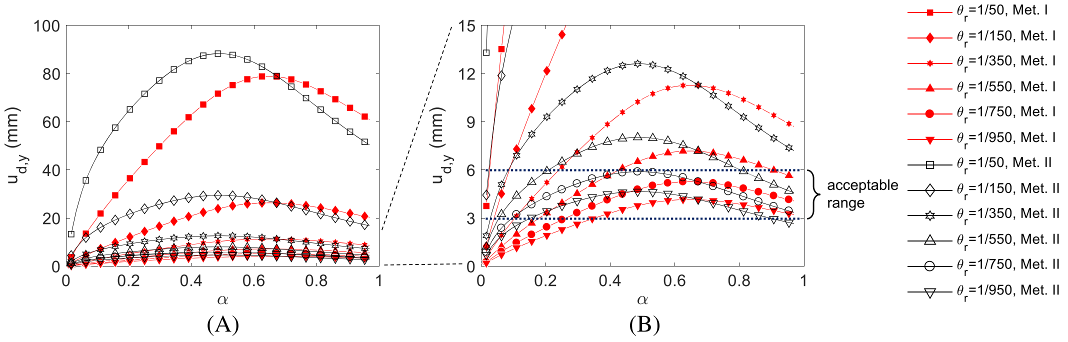

(A) (B)

FIGURE 12 A, Relationships between $u_{d,y}$ and α for different θ_r of 32-story model and B, enlargement [Colour figure can be viewed at wileyonlinelibrary.com]

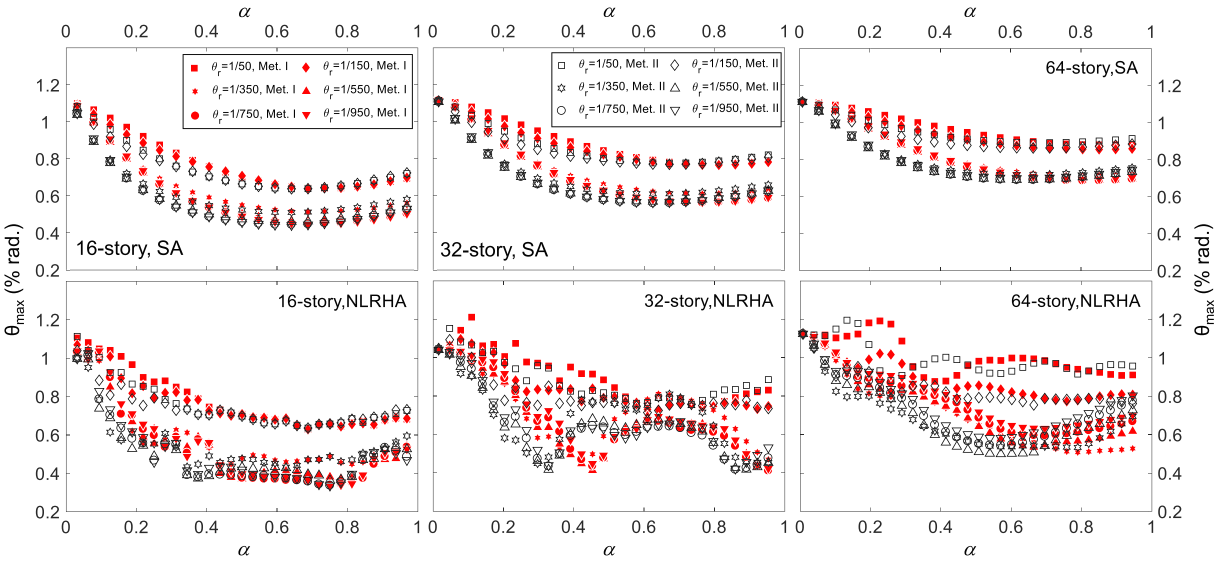

FIGURE 13 Relationship between $\theta_{\max}$ and α for different θ_r of 16, 32, and 64-story models as obtained from spectral analysis and nonlinear response history analysis [Colour figure can be viewed at wileyonlinelibrary.com]

same as used in the first analysis, except that R_{dt} varies between 0.05 and 0.9. As k_g remains constant with varying α in Met. I, varying R_{dt} does not affect the analysis result. The second analyses were performed by using Met. II only.

Figure 12 shows the relationship between $u_{d,y}$ and α. A larger θ_r leads to a larger $u_{d,y}$. For a given θ_r, the maximum value of $u_{d,y}$ is obtained when α is approximately 0.6 to 0.7 in Met. I and 0.5 in Met. II. In design practices, $u_{d,y}$ should lie in a reasonable range (eg, 1/1000 of the BRB length). In the example structure, the BRB is arranged vertically in a story with a height of 4 m; therefore, $u_{d,y}$ should be approximately 3 to 6 mm. Figure 13 shows the relationship between $\theta_{\max}$ and α for different θ_r as obtained from SA and NLRHA. The trends of maximum roof drift ratio variations with respect to α obtained from both SA and NLRHA are similar. However, these trends differ slightly from the 32-story model's analytical results in certain period ranges. This could be because, for periods other than the first mode, the BCJ-L2 spectral accelerations are considerably greater than the design spectral acceleration. Figure 14 shows the relationship between θ_r and α when minimum $\theta_{\max}$ is achieved. The corresponding $\theta_{\max}$ of each point is also shown in Figure 14. Although the SA results correlated well with the NLRHA results for the 16- and 64-story models, as shown in Figures 13 and 14, both the SA and NLRHA results suggest that a smaller θ_r best reduces $\theta_{\max}$, and the BRBs start dissipating energy in a relatively small lateral deformation of the building. However, for θ_r values smaller than 1/550, the reduction in $\theta_{\max}$ was not large enough to significantly improve the performance. The ratio of BRB's cumulative plastic deformation to axial yield deformation (R_{CPD})[18] is adopted to indicate the ductility demand for the BCJ-L2 ground motion. Figure 15 shows the R_{CPD} obtained from the NLRHA results. When θ_r is greater than 1/150, the relatively small R_{CPD} suggest that the BRBs have low energy dissipation efficiency or deform elastically (when $R_{\text{CPD}} = 0$) as a traditional outrigger system. However, when θ_r is smaller than 1/950, the large R_{CPD} may not be practically achieved in conventional BRBs. Therefore, from the above analysis results, $\theta_r = 1/750$ results in an acceptable range of $u_{d,y}$ (from 3 to 6 mm, for example) and R_{CPD} values for the example model. For the design practices, θ_r can be determined by code specified maximum allowable elastic roof drift ratio. As indicated in Equation (16), $u_{d,y}$ is affected not only by θ_r but also by α and l_t. Thus, in design practices, θ_r should be properly defined based on the actual building configuration.

Figure 16 shows the relationship between $u_{d,y}$ and α under different R_{dt}. The ranges of $u_{d,y}$ differences because of varying R_{dt} (around 3 mm) are much smaller than varying θ_r (more than 20 mm, Figure 12). Figure 17 shows the relationships between the first to fourth mode vibration periods and α for different R_{dt}. Figure 18 shows the relationship between $\theta_{\max}$ and α as obtained from SA and NLRHA. Because k_t is much greater than k_d and k_c, changing R_{dt} only slightly affects k_g. Thus, the changes in dynamic characteristics and the maximum responses of the overall system because of the variation

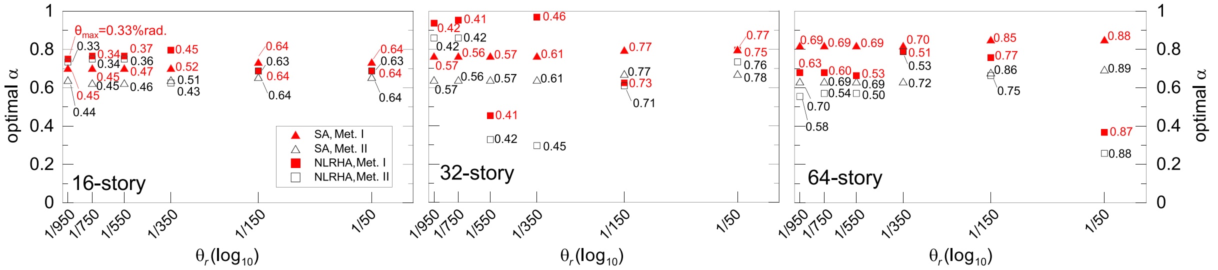

FIGURE 14 Relationships between optimal α and θ_r of 16, 32, and 64-story models as obtained from spectral analysis and nonlinear response history analysis [Colour figure can be viewed at wileyonlinelibrary.com]

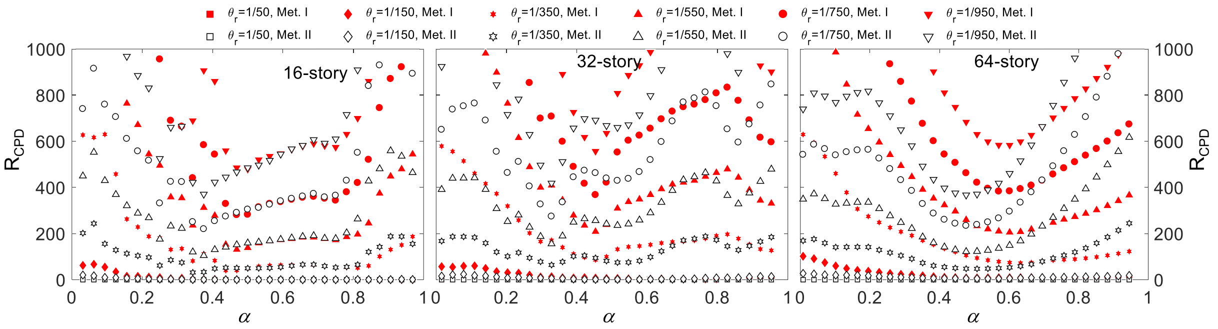

FIGURE 15 Relationships between R_{CPD} and α for different θ_r of 16, 32, and 64-story models as obtained from nonlinear response history analysis [Colour figure can be viewed at wileyonlinelibrary.com]

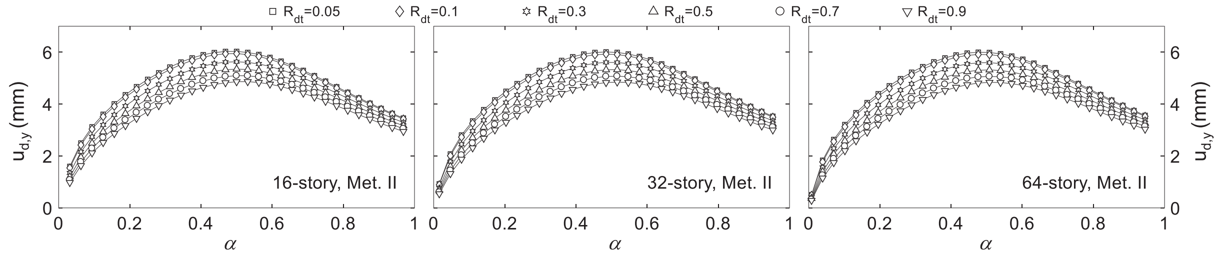

FIGURE 16 Relationships between $u_{d,y}$ and α for different R_{dt} of 16, 32, and 64-story models

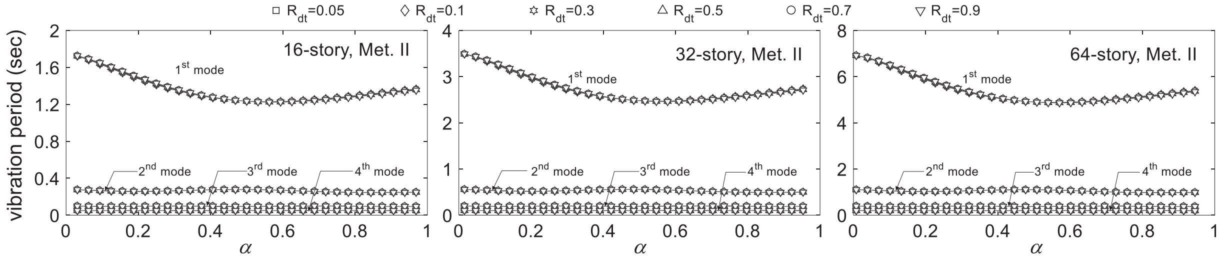

FIGURE 17 Relationships between vibration period and α for different R_{dt} of 16, 32, and 64-story models

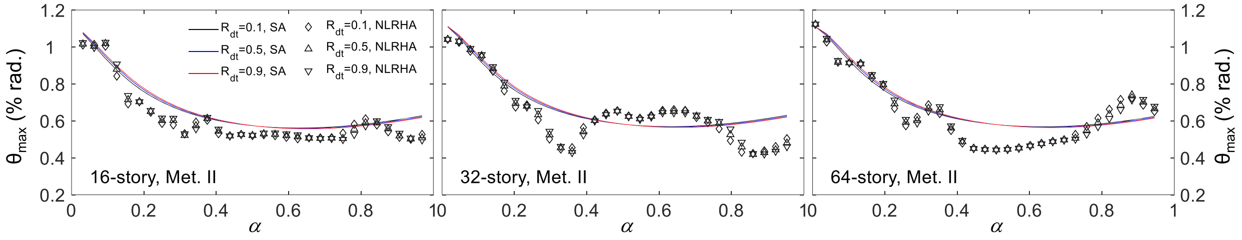

FIGURE 18 Relationships between $\theta_{\max}$ and α for different R_{dt} of 16, 32, and 64-story models as obtained from spectral analysis and nonlinear response history analysis [Colour figure can be viewed at wileyonlinelibrary.com]

in R_{dt} (ranging from 0.05 to 0.9) are insignificant. For the design practices, the $u_{d,y}$ can be fine-tuned by changing R_{dt} so that $u_{d,y}$ lies within a desirable range. R_{dt} is fixed at 0.1 for further analysis in the following sections.

4.2 | Investigation of optimal α, R_{db}, and R_{dc}

In this section, the optimal α, R_{db}, and R_{dc} to achieve the minimum $\theta_{\max}$ are investigated. Figure 19 shows the relationship between the first to the third mode periods and α for different R_{db} (Met. I) and R_{dc} (Met. II). It should be noted that Met. I fixes R_{db} as constant while changing α, so the corresponding R_{dc} varies with the changing α. Likewise, the Met. II fixes R_{dc} as constant, and the corresponding R_{db} varies with α. Increasing R_{db} (Met. I) or R_{dc} (Met. II) stiffens the system and causes the vibration periods to decrease. Under the same set of S_{bc}, and R_{db} or R_{dc}, when α is between 0.5 and 0.8, the outrigger effect on the system is significant because the first mode period becomes minimum within this α range. The α that results in the smallest first mode period is higher for taller structure model in Met. I (when S_{bc} is smaller) but almost remains unchanged in Met. II. In addition, increasing R_{db} or R_{dc} enhances the outrigger effect and thus results in smaller vibration periods.

Figure 20 shows the relationships between $\theta_{\max}$ and α under various R_{db} (Met. I) and R_{dc} (Met. II) as obtained from SA and NLRHA. Both the SA and NLRHA results show similar trends. Based on the analytical results, for a given set of R_{db} or R_{dc}, $\theta_{\max}$ becomes minimum when α is approximately between 0.7 and 0.8 for Met. I, and from 0.5 to 0.7 for Met. II. In addition, the Met. I results indicate that the optimal α value is higher for taller structure model (when S_{bc} is smaller). The trend of $\theta_{\max}$ with respect to α is similar to the first mode period trend as shown in Figure 19. This suggests that the outrigger elevation that has greatest outrigger effect on the system is also the optimal elevation to achieve

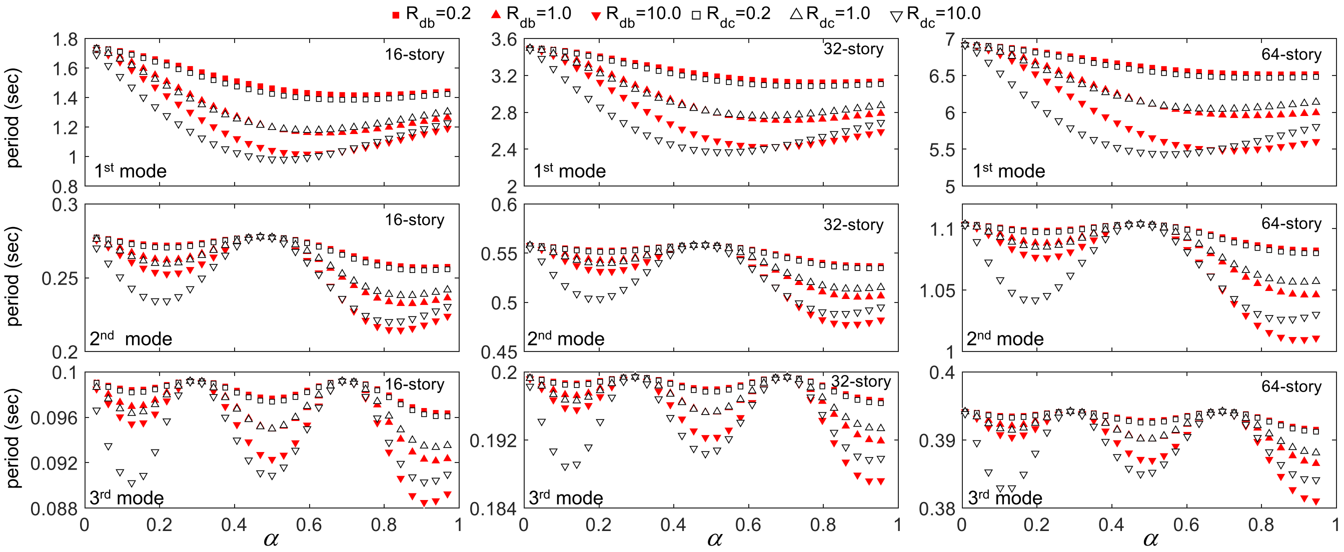

FIGURE 19 Relationships between the first to third mode periods and α for different R_{db} and R_{dc} of 16, 32, and 64-story models [Colour figure can be viewed at wileyonlinelibrary.com]

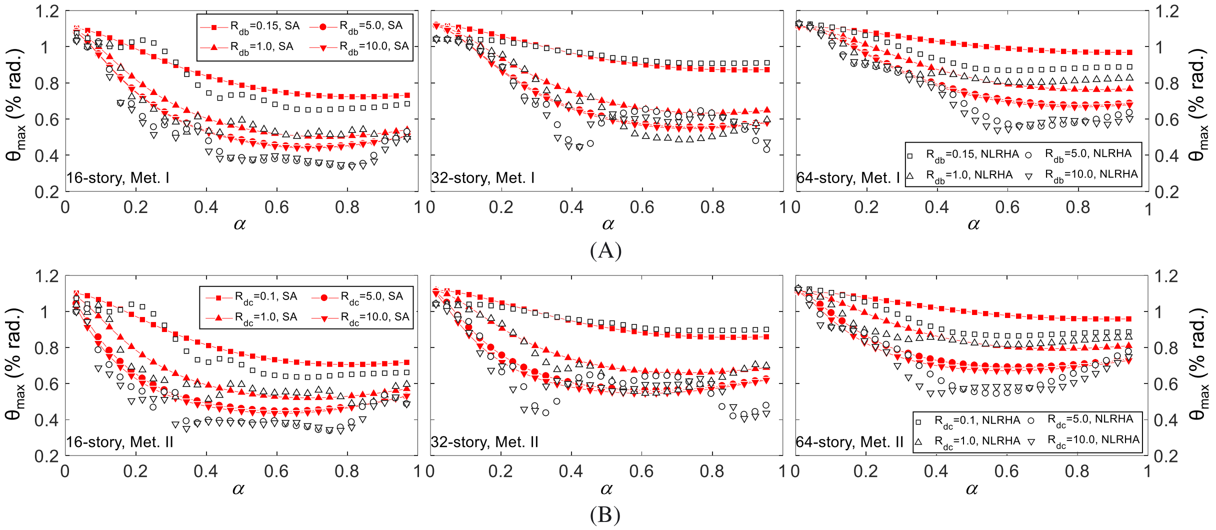

FIGURE 20 Relationships between $\theta_{\max}$ and α for various A, R_{db} and B, R_{dc} of 16, 32, and 64-story models as obtained from spectral analysis and nonlinear response history analysis. [Colour figure can be viewed at wileyonlinelibrary.com]

minimum $\theta_{\max}$. Figure 20 also shows that larger R_{db} and R_{dc} lead to smaller $\theta_{\max}$. However, both SA and NLRHA show that $\theta_{\max}$ obtained when R_{db} equals 5.0 and 10.0, and when R_{dc} equals 5.0 and 10.0, are very close to each other. This suggests that a stiffer BRB (larger R_{db} or R_{dc}) does not guarantee a better performance in reducing $\theta_{\max}$.

Figure 21 shows the minimum $\theta_{\max}$ and its corresponding R_{db} or R_{dc} from each analysis set. Larger R_{db} or R_{dc} value results in greater reductions in $\theta_{\max}$; however, the reductions stop increasing when R_{db} or R_{dc} is greater than around 2, 3, and 5 for the 16, 32, and 64-story model, respectively. Figures 22 and 23 show R_{CPD} and the relationship between ratios of energy dissipated by BRBs to the total input energy with respect to α, computed from the NLRHA results. The R_{CPD} begins increasing significantly when R_{db} and R_{dc} are greater than 5.0. For the models with large R_{db} or R_{dc} values, once the BRB yields, the drop in BRB stiffness from k_d to relatively small postyield stiffness (pk_d), if compared with k_c and k_t, can result in large deformation concentration in the BRB. In addition, as illustrated in section 2.3, large R_{db} or R_{dc} would result in smaller $u_{d,y}$. Thus, the energy dissipation efficiencies for the models with large R_{db} or R_{dc} values (small $u_{d,y}$) accompanied with large BRB axial deformation may be similar to those with small R_{db} or R_{dc} value that lies between 3 and 5. This explains that when R_{db} or R_{dc} is larger, $\theta_{\max}$ cannot be proportionally reduced and the

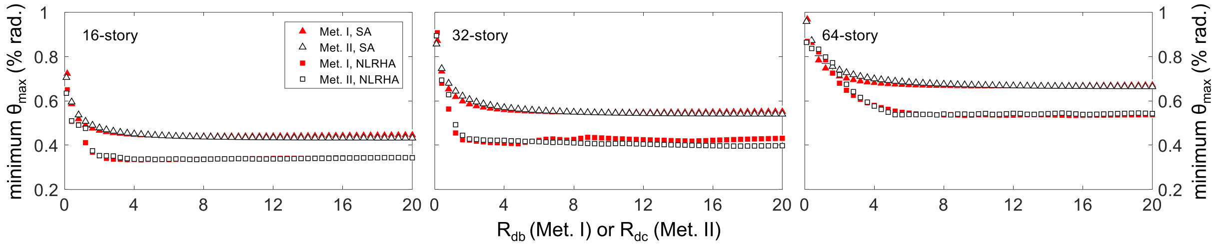

FIGURE 21 Relationships between $\theta_{\max}$ and R_{db} (Met. I) or R_{dc} (Met II.) of 16, 32, and 64-story models [Colour figure can be viewed at wileyonlinelibrary.com]

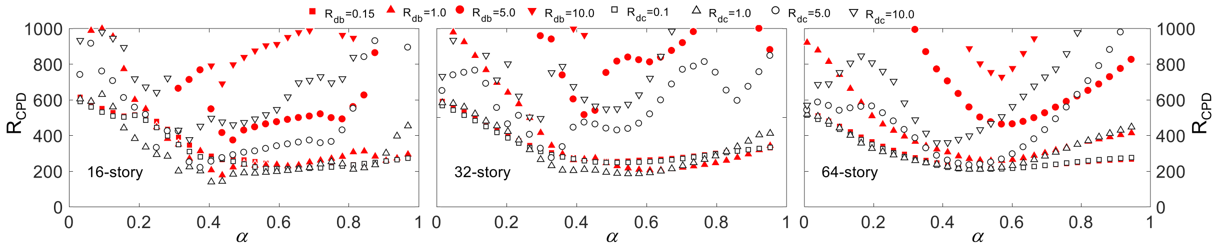

FIGURE 22 Relationships between R_{CPD} and α for various R_{db} or R_{dc} of 16, 32, and 64-story models as obtained from nonlinear response history analysis [Colour figure can be viewed at wileyonlinelibrary.com]

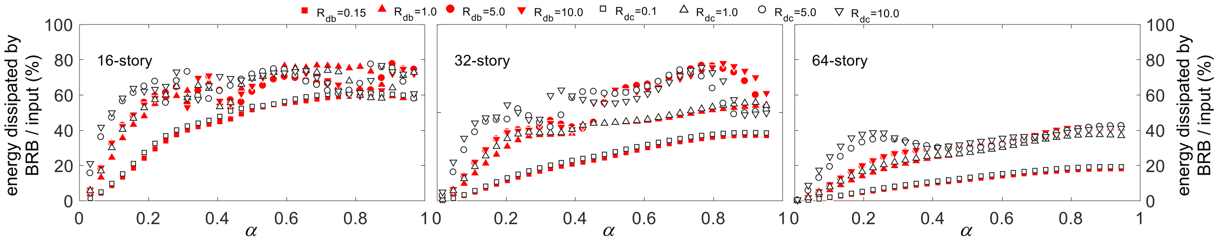

FIGURE 23 Relationships between the ratio of energy dissipated by buckling-restrained brace to input energy and α for various R_{db} or R_{dc} of 16, 32, and 64-story models as obtained from nonlinear response history analysis [Colour figure can be viewed at wileyonlinelibrary.com]

BRB energy dissipation efficiency remains almost the same. This also explains the large R_{CPD} found from the models with large R_{db} or R_{dc} values. However, a very large R_{CPD} value indicates that the BRB may use up its ductility capacity and eventually fracture before the end of earthquake, which is not desirable for engineering practices. For the design purpose, increasing R_{db} or R_{dc} also increases the cost of BRB and may reduce the BRB use life. Based on the analysis results, to reduce $\theta_{\max}$ and let the BRB to properly function at the same time, it is suggested that the R_{db} and R_{dc} should be greater than 1 and smaller than 5.

The reduction factors of $\theta_{\max}$ (R_d) and $a_{\max}$ (R_{pa}), if compared with the structure without the outrigger, can be calculated as follows:

$$R_d = \frac{S_d\left(T_{eq,1},\ h_{eq,1}\right)}{S_d\left(T_0,\ h_0\right)} = D_{h,1}\frac{T_{eq,1}S_{pv}\left(T_{eq,1},\ h_0\right)}{T_0\ \ S_{pv}\left(T_1,\ h_0\right)}, \qquad R_{pa} = \frac{S_{pa}\left(T_{eq,1},\ h_{eq,1}\right)}{S_{pa}\left(T_n,\ h_0\right)} = D_{h,1}\frac{T_0\ \ S_{pv}\left(T_{eq,1},\ h_0\right)}{T_{eq,1}\ \ S_{pv}\left(T_0,\ h_0\right)} \tag{21}$$

where T_0 is the linearly elastic fundamental period of the core structure only. As the fundamental mode dominates the building responses, the R_d and R_{pa} calculations consider the contribution of first mode only. Figures 24 and 25 show the relationships between R_{pa} and R_d (performance curves) with fixed α and fixed R_{db} or R_{dc}. The numbers in Figure 24 indicate the corresponding R_{db} (Met. I) or R_{dc} (Met. II), and the numbers in Figure 25 indicate the corresponding α.

From both Figures 24 and 25, both R_d and R_{pa} reach minima when α is between 0.5 and 0.7. Met. I results show that the optimal α value, to achieve minimum R_{pa} and R_d, increases from around 0.5 to 0.7 with increasing building height

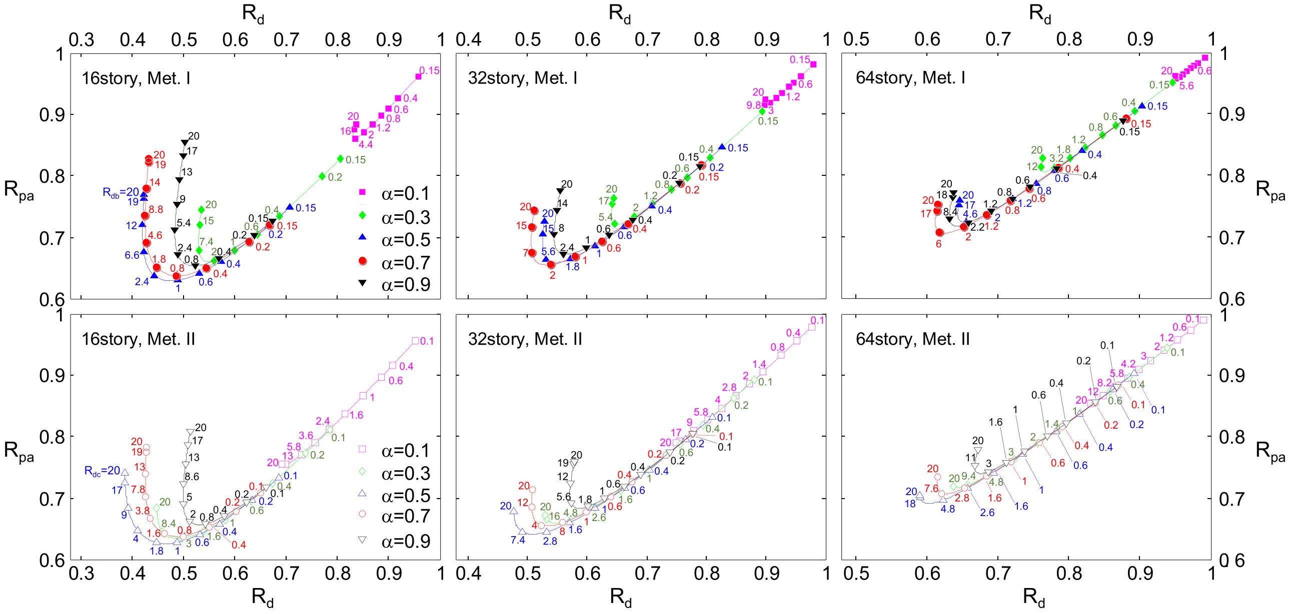

FIGURE 24 Performance curves of Met. I and Met. II with fixed α of 16, 32, and 64-story models [Colour figure can be viewed at wileyonlinelibrary.com]

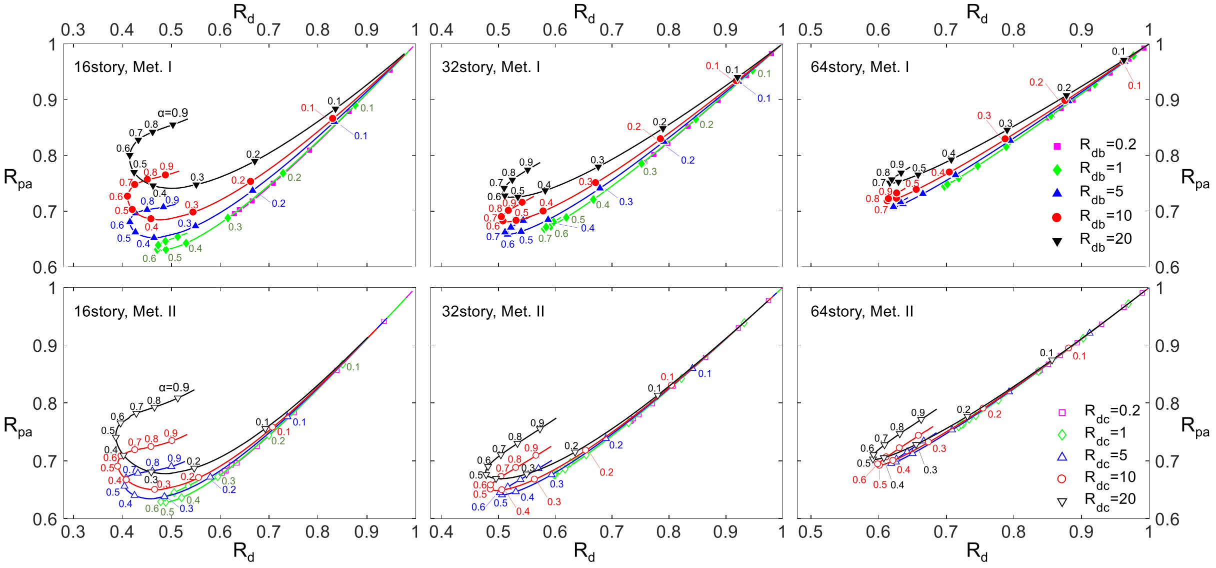

FIGURE 25 Performance curves of Met. I and Met. II with fixed R_{db} or R_{dc} of 16, 32, and 64-story models [Colour figure can be viewed at wileyonlinelibrary.com]

(decreasing S_{bc}). In addition, for any fixed α, the $\theta_{\max}$ can be reduced by increasing R_{db} or R_{dc}. However, if R_{db} or R_{dc} is too large resulting in a very stiff system, R_{pa} could be significantly amplified, and R_d could increase again. As shown in Figure 25, when R_{db} or R_{dc} is fixed and when the outrigger elevation is higher than optimal α, both $\theta_{\max}$ the $a_{\max}$ could increase. Table 7 shows the α, R_{db}, or R_{dc} when minimum R_d or R_{pa} is achieved. The optimal α required to achieve minimum R_d and R_{pa} is approximately 0.6 (16-story), 0.65 (32-story), and 0.7 (64-story) for Met. I and 0.5 for Met. II. As shown in Figure 24, The R_{db} or R_{dc} for achieving minimum R_{pa} could result in R_d that is close to its minimum. Thus, the optimal R_{db} and R_{dc} could be approximated from the minimum R_{pa} value. If compared the analysis results with 3 types of S_{bc} values in Met. I, increasing S_{bc} (increasing k_b) should be more efficient than increasing R_{db} or R_{dc} to enhance the outrigger effect because the large R_{db} and R_{dc} could amplify $a_{\max}$. Based on the analytical results, the design with α

TABLE 7 α, S_{bc}, R_{db}, and R_{dc} at minimum R_d and R_{pa} with R_{db} or R_{dc} ranges from 0.1 to 20.0

		To Achieve Minimum R_d					**To Achieve Minimum R_{pa}**				
Model	**Met.**	α	S_{bc}	R_{db} **or** R_{dc}	R_d	R_{pa}	α	S_{bc}	R_{db} **or** R_{dc}	R_d	R_{pa}
16-story	I	0.58	3.03	10.2	0.41	0.72	0.50	3.03	1.2	0.48	0.63
	II	0.50	4.23	20.0	0.39	0.74	0.45	4.48	1.6	0.47	0.62
32-story	I	0.64	1.38	11.0	0.50	0.69	0.61	1.38	2.6	0.53	0.65
	II	0.52	1.89	20.0	0.48	0.68	0.48	1.97	4.6	0.51	0.64
64-story	I	0.71	0.66	11.2	0.61	0.72	0.70	0.66	4.4	0.62	0.70
	II	0.52	0.89	20.0	0.59	0.71	0.51	0.90	8.4	0.60	0.69

that lies between 0.5 and 0.8, R_{db} (Met. I) and R_{dc} (Met. II) that lie around 1 when S_{bc} is between 2 and 5, 3 when S_{bc} is between 1 and 2, and 4 when S_{bc} is less than 1 could achieve satisfactory results in reducing both $\theta_{\max}$ and $a_{\max}$ responses.

4.3 | Verification of optimal design by NLRHA

The proposed optimal design parameters are examined by performing NLRHA with the original observed ground motions listed in Table 5. The response spectra are shown in Figure 8A. Figure 26 shows the relationship between $\theta_{\max}$ and α. R_{db} and R_{dc} are set to 1, 3, and 4, for the 16, 32, and 64-story model, respectively. In most cases, the optimal α lies between 0.5 and 0.8. However, the optimal α for the 32 and 64-story models correspond to the building top and bottom for Kumamoto, KobeJMA, and Sendai ground motions. This could be because the second mode responses are amplified because of the relatively large spectral accelerations of those ground motions corresponding to the second mode period, if compared with the design spectrum. And the optimal outrigger elevations (optimal α) are close to the α that results in the smallest second mode period as shown in Figure 19. Based on the NLRHA results, when the outrigger is placed at the optimal location, the $\theta_{\max}$ is found to be reduced by 42% for the 16-story model, 24% for the 32-story model, and 22% for the 64-story model, respectively, on average.

Figure 27 shows the relationships between $\theta_{\max}$ and R_{db} or R_{dc}, where the α is set to 0.7 in each analysis. Because both R_{db} and R_{dc} directly affect structure stiffness, the relationships between $\theta_{\max}$ and R_{db} or R_{dc} vary with ground motions. Figure 27 also shows trend similar to Figure 21; $\theta_{\max}$ cannot be further reduced or even amplified when R_{db} or R_{dc} is too large. The optimal R_{db} and R_{dc} values for 16-story model are larger than 1.0 for the Tohoku, Taft, and Sendai ground motions. This could be because 16-story model with larger S_{bc} and shorter fundamental period is more sensitive to the variations in ground motions. However, the optimal R_{db} and R_{dc} values for all analytical results lie in the range of 1 to 5.

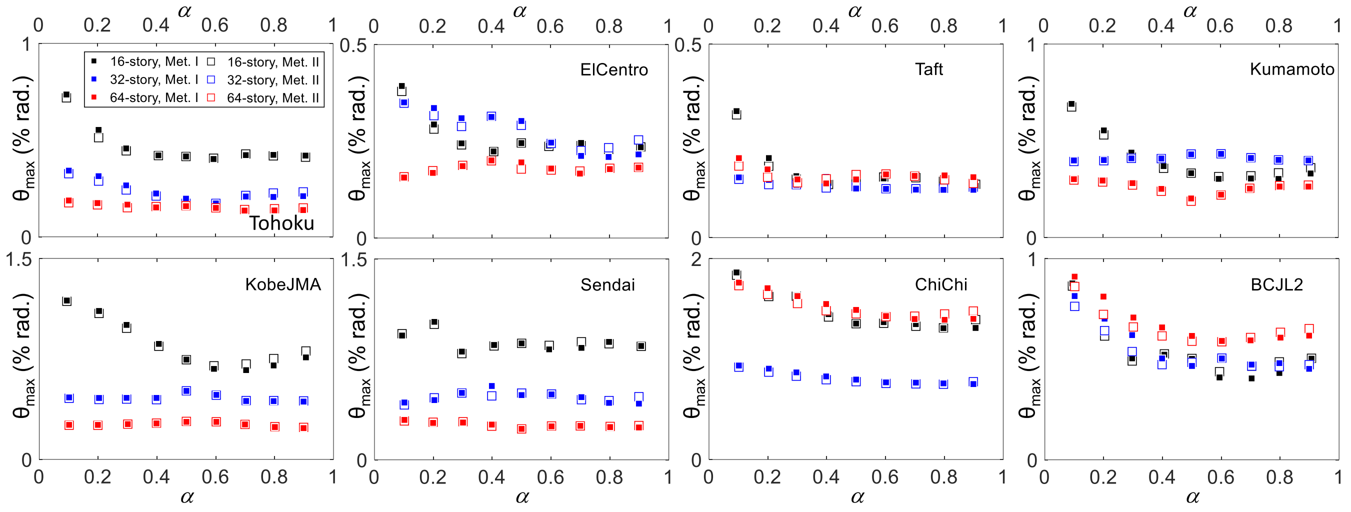

FIGURE 26 Relationships between $\theta_{\max}$ and α of nonlinear response history analysis results with original observed earthquakes [Colour figure can be viewed at wileyonlinelibrary.com]

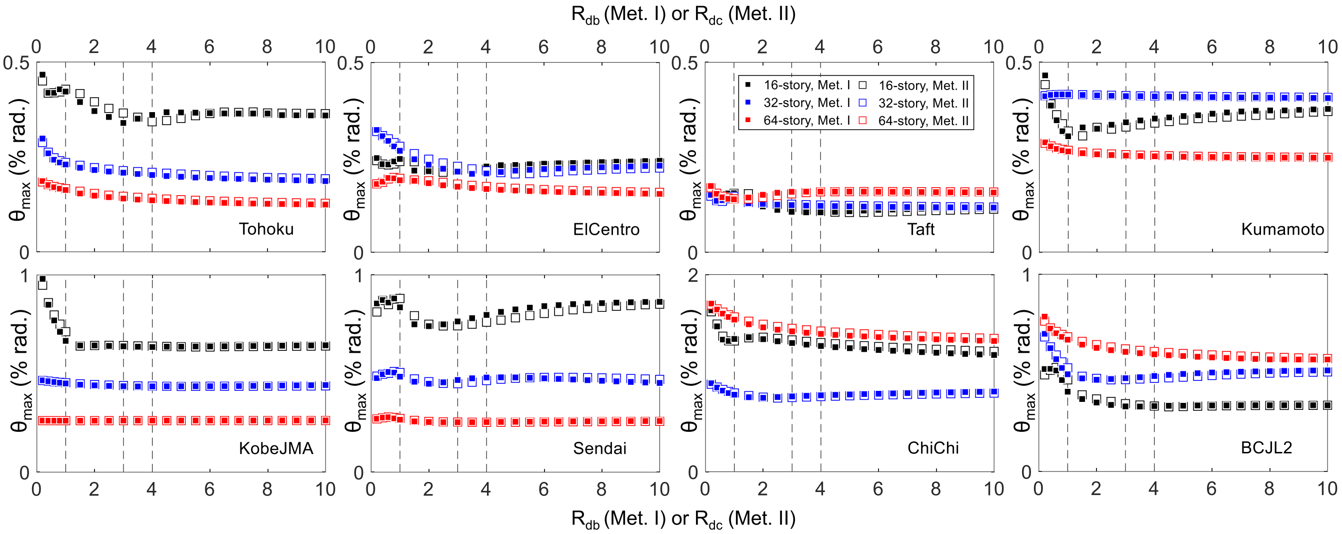

FIGURE 27 Relationships between θ_{max} and R_{db} or R_{dc} of nonlinear response history analysis results with original observed earthquakes [Colour figure can be viewed at wileyonlinelibrary.com]

4.4 | Design recommendation

The optimal values of α, R_{db}, and R_{dc} to minimize R_d and R_{pa} were investigated. Figure 28 shows a recommended design flow chart. For design practice, the building lateral stiffness (core structure flexural rigidity, *EI*) should be determined based on the code specifications. The perimeter column sizes (k_c) should be determined according to floor framing plan and gravity load demands. Thus, k_d and k_t may be less restrained. Smaller k_d (smaller R_{db} and R_{dc}) and k_t are desirable because they reduce material usage and cost. Based on the analytical results, the recommended design procedure is as follows:

(1) If α is not restricted for architectural reasons, select α between 0.6 and 0.8.
(2) Target S_{bc} to lie in the range of 2.0 to 5.0, as larger S_{bc} leads to smaller optimal R_{db} and R_{dc}.
(3) Compute k_t according to the S_{bc} determined in the previous step. If k_t is too large to design the outrigger truss members, reduce k_t until the outrigger truss member sizes are reasonable and recompute S_{bc}.
(4) Select Met. I if the perimeter column sizes are adjustable; otherwise, select Met. II. Target the optimal R_{db} (Met. I) or R_{dc} (Met. II) according to the S_{bc}.
(5) Compute k_d based on the selected optimal R_{db} or R_{dc}.

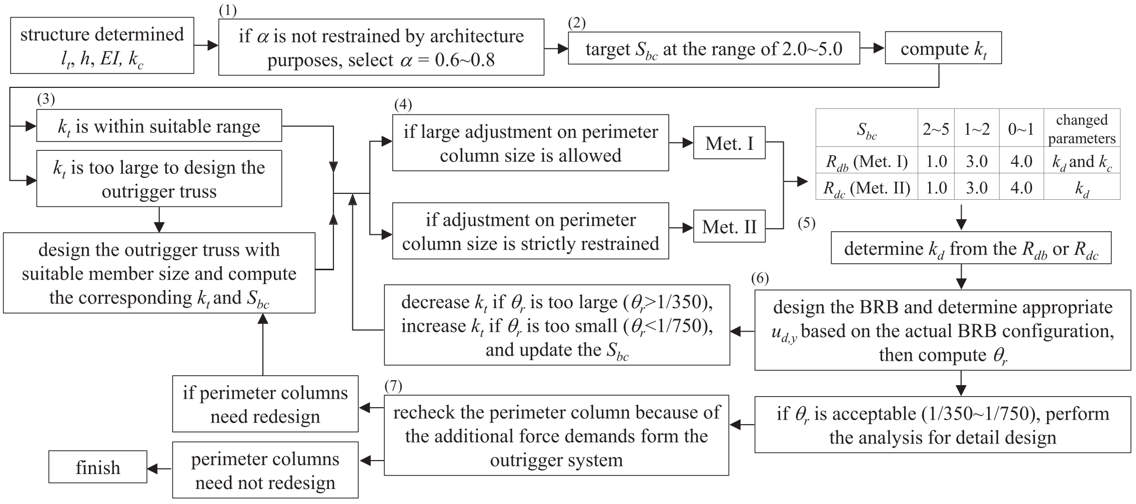

FIGURE 28 Flow chart of design recommendation

(6) Design the BRB based on the k_d computed in Step (5). Determine appropriate $u_{d,y}$ based on the actual BRB configuration and calculate the corresponding θ_r by performing pushover analysis. Decrease k_t if θ_r is too large ($\theta_r > 1/350$) or increase k_t if θ_r is too small ($\theta_r < 1/750$) until the θ_r is within a reasonable range (eg, 1/350 to 1/750).

(7) After all the parameters are determined, perform the analysis and proceed to member design. As the outrigger would lead to additional force demands on the perimeter column, the perimeter column design should include the effect of possible maximum BRB axial force.

5 | CONCLUSIONS

This study proposed a simplified structure to evaluate the seismic behavior of buildings with BRB-outrigger systems. The methods to determine the BRB yield deformation, and the optimal stiffness relationships among the core structure, BRB, outrigger truss, and the perimeter columns were discussed. Based on the analytical results, the following conclusions can be drawn:

(1) Three types of analytical models were adopted in this study. The UM was used when performing SA, and DM1 was used when performing NLRHA. The analytical results of simplified structure using UM, DM1, and DM4 models were in good agreement with the results obtained from MBM models.

(2) SA was adopted to investigate the optimal α, R_{db}, and R_{dc} values to achieve minimum roof drift ratio and acceleration responses. The SA incorporated the equivalent damping induced from BRB's inelastic deformation, and the results were verified by performing NLRHA. Both the SA and NLRHA results showed similar trends with various α, R_{db}, and R_{dc}.

(3) The BRB's yield deformation should be appropriately determined. A very large $u_{d,y}$ would reduce the BRB's energy dissipation efficiency. The BRB with very small $u_{d,y}$ could easily yield during minor earthquakes or use up its ductility capacity before the end of a large earthquake.

(4) Based on the analytical results, the first mode response dominates the seismic behavior. It is suggested to determine $u_{d,y}$ from the BRB's axial deformation in the first mode when roof drift reaches elastic deformation limit (1/750 for example).

(5) Two methods were developed in this study. In Met. I, the rotational stiffness resulting from the outrigger is kept constant while changing α. In Met. II, k_c remains constant, and thus, k_g decreases with increasing α. Based on the analysis results, $\theta_{\max}$ can be reduced best when α is between 0.6 and 0.8 for Met. I and between 0.5 and 0.6 for Met. II.

(6) Based on the analytical results, the optimal α values were not found to be significantly affected by either R_{db} or R_{dc}. Larger R_{db} and R_{dc} resulted in greater efficiency in reducing $\theta_{\max}$. However, the maximum acceleration response would be amplified if R_{db} and R_{dc} are too large. The optimal R_{db} and R_{dc} values to achieve minimum $\theta_{\max}$ and $a_{\max}$ are approximately 1 for S_{bc} ranging from 2 to 5, 3 for S_{bc} ranging from 1 to 2, and 4 for S_{bc} smaller than 1.

(7) According to the results of NLRHA on the models with and without optimal design parameters, the ones with optimal α could reduce the $\theta_{\max}$ by 42%, 24%, and 22% for the 16, 32, and 64-story models, respectively. The optimal R_{db} and R_{dc} values lie within the range of 1 to 5.

ORCID

Pao-Chun Lin http://orcid.org/0000-0001-5389-5192

REFERENCES

1. Poon D., Shieh SS., Joseph L., Chang CC. Structural design of Taipei 101, the world's tallest building. Proceedings of the CTBUH Seoul Conference; 2004:217–278.

2. Lu X, Zou Y, Lu W, Zhao B. Shaking table model test on Shanghai World Financial Center Tower. *Earthq Eng Struct Dyn*. 2007;36(4):439-457.

3. Viise J, Ragan P, Swanson J. BRB and FVD alternatives to conventional steel brace outriggers. Proceedings of the CTBUH Shanghai Conference; 2014:691–699.

4. Huang B, Takeuchi T. Dynamic response evaluation of damped-outrigger systems with various heights. *Earthq Spectra*. 2017;33(2):665-685.
5. Chen Y, McFarland D, Wang Z, Spencer B, Bergman L. Analysis of tall building with damped outriggers. *J Struct Eng*. 2010;136(11):1435-1443.
6. Tan P, Fang C, Zhou F. Dynamic characteristics of a novel damped outrigger system. *Earthq Eng Eng Vib*. 2014;13(2):293-304.
7. Smith R, Willford M. The damped outrigger concept for tall buildings. *Struct Design Tall Spec Build*. 2007;16(4):501-517.
8. Tan P, Fang CJ, Tu WR, Zhou FL, Wang Y, Jiang M. Experimental study on the outrigger damping system for high-rise building. Proceedings of the 15th World Conference on Earthquake Engineering, Lisbon, Portugal; 2012.
9. Wu JR, Li QS. Structural performance of multi-outrigger-braced tall buildings. *Struct Design Tall Spec Build*. 2003;12(2):155-176.
10. Willford M, Smith R. Performance based seismic and wind engineering for 60 story twin towers in Manila. Proceedings of the 14th World Conference on Earthquake Engineering, Beijing, China; 2008.
11. Watanabe A, Hitomi Y, Saeki E, Wada A, Fijimoto M. Properties of brace encased in buckling-restraining concrete and steel tube. Proceedings of the 9th World Conference on Earthquake Engineering, vol. 4, Tokyo, Japan; 1988.
12. Joseph L, Gulec K, Schwaiger J. Wilshire grand: outrigger designs and details for a highly seismic site. *Int J High-Rise Buildings*. 2016;5(1):1-12.
13. Infanti S, Robinson J, Smith R. Viscous dampers for high-rise buildings. Proceedings of the 14th World Conference on Earthquake Engineering, Beijing, China; 2008.
14. Chopra A, Goel R. A modal pushover analysis procedure for estimating seismic demands for buildings. *Earthq Eng Struct Dyn*. 2002;31(3):561-582.
15. McKenna F. Object oriented finite element programming frameworks for analysis, algorithms and parallel computing. Ph.D. thesis, University of California, Berkeley; 1997.
16. OpenSees command manual. http://opensees.berkeley.edu/wiki/index.php/Command_Manual.
17. Lin BZ, Chuang MC, Tsai KC. Object-oriented development and application of a nonlinear structural analysis framework. *Adv Eng Softw*. 2009;40(1):66-82.
18. American Institute of Steel Construction (AISC). Seismic provisions for structural steel buildings, Chicago, Illinois, U.S.A.; 2016a.
19. Takeuchi T, Wada A. *Buckling-Restrained Braces and Application*. Tokyo, Japan: Japan Society of Seismic Isolation (JSSI); 2017.
20. American Institute of Steel Construction (AISC). Specification for structural buildings, Chicago, Illinois, U.S.A.; 2016b.
21. Kasai K, Fu Y, Watanabe A. Passive control system for seismic damage mitigation. *J Struct Eng*. 1998;124(5):501-512.
22. Newmark M, Rosenblueth E. *Fundamentals of Earthquake Engineering*. Englewood Cliffs, N.J., U.S.A.: Prentice-Hall, Inc.; 1971.
23. Shome N, Cornell CA. Normalization and scaling accelerograms for nonlinear structural analysis, Sixth U.S. National Conference on Earthquake Engineering, Seattle, WA; 1998.

How to cite this article: Lin P-C, Takeuchi T, Matsui R. Seismic performance evaluation of single damped-outrigger system incorporating buckling-restrained braces. *Earthquake Engng Struct Dyn*. 2018;47:2343–2365. https://doi.org/10.1002/eqe.3072